

Investigating electrolyte and charge rate effects on the sodiation of hard carbon

A combined SAXS and electrochemical study on sodium-ion batteries

Master's thesis in Physics

ISAK DREVANDER

DEPARTMENT OF PHYSICS

CHALMERS UNIVERSITY OF TECHNOLOGY
Gothenburg, Sweden 2024
www.chalmers.se

MASTER'S THESIS 2024

Investigating electrolyte and charge rate effects on the sodiation of hard carbon

A combined SAXS and electrochemical study on sodium-ion batteries

ISAK DREVANDER



Department of Physics
Division of Materials Physics
CHALMERS UNIVERSITY OF TECHNOLOGY
Gothenburg, Sweden 2024

Investigating electrolyte and charge rate effects on the sodiation of hard carbon
A combined SAXS and electrochemical study on sodium-ion batteries
ISAK DREVANDER

© ISAK DREVANDER, 2024.

Supervisor: Martina Olsson, Department of Physics, Chalmers University of Technology, Gothenburg
Examiner: Aleksandar Matic, Department of Physics, Chalmers University of Technology, Gothenburg

Master's Thesis 2024
Department of Physics
Division of Materials Physics
Chalmers University of Technology
SE-412 96 Gothenburg
Telephone +46 31 772 1000

Cover: Schematic overview of a sodium-ion battery, with hard carbon particles visualized on the anode. The hierarchical structure of hard carbon, along with possible storage sites for sodium ions, are also visible in the figure.

Typeset in L^AT_EX
Printed by Chalmers Reproservice
Gothenburg, Sweden 2024

Investigating electrolyte and charge rate effects on the sodiation of hard carbon
A combined SAXS and electrochemical study on sodium-ion batteries
ISAK DREVANDER
Department of Physics
Chalmers University of Technology

Abstract

The interest in sodium-ion batteries has exponentially increased in the past 15 years. One of the challenges in developing this technology has been in finding suitable anode materials. As of today the most promising candidate is hard carbon. The material is often defined as a non-graphitizable form of carbon that lack long-range order, and is made up of deformed and disarranged sheets of graphene. Due to the complex amorphous structure, which can vary depending on the fabrication process, there is currently no consensus regarding the sodium storage mechanism in the material. By achieving a better understanding of this process, the nanoscale structure of hard carbon anodes could be engineered to enhance its storage capabilities.

In this study, the sodiation process in hard carbon anodes was studied using small- and wide-angle X-ray scattering along with electrochemical characterization techniques. Two charge rates (C/5 and C/10) and two electrolytes (one ester-based and one ether-based) have been compared to investigate possible variations in sodium storage mechanisms. In all configurations, the scattering results show signatures of pore filling occurring during the whole sodiation process while signatures from intercalation appears first at higher degree of sodiation. This suggests that pore filling takes place during the sloping region of the voltage profile, while the two mechanisms occur simultaneously in the plateau region. The pore filling mechanism was less dominant when using a higher charge rate, and more intercalation was observed in batteries using an ether-based electrolyte than those with an ester-based electrolyte.

Keywords: Sodium-ion batteries, hard carbon, SAXS, sodiation, charge rate, electrolyte, diglyme, EC:PC

Acknowledgements

Lorem ipsum dolor sit amet, consectetur adipisicing elit, sed do eiusmod tempor incididunt ut labore et dolore magna aliqua. Ut enim ad minim veniam, quis nostrud exercitation ullamco laboris nisi ut aliquip ex ea commodo consequat. Duis aute irure dolor in reprehenderit in voluptate velit esse cillum dolore eu fugiat nulla pariatur. Excepteur sint occaecat cupidatat non proident, sunt in culpa qui officia deserunt mollit anim id est laborum.

Isak Drevander, Gothenburg, June 2024

Contents

List of Acronyms	xi
List of Figures	xiii
List of Tables	xvii
1 Introduction	1
2 Batteries	3
2.1 The electrochemical cell	4
2.2 Electrochemical characterization techniques	6
2.3 Anode materials in SIBs	7
2.4 Electrolytes in SIBs	7
3 Hard carbon	9
3.1 Structure and synthesis	10
3.2 Sodium storage mechanisms in hard carbon	11
4 S/WAXS analysis	15
4.1 Basic principles of S/WAXS	16
4.2 Studying hard carbon sodiation with S/WAXS	17
5 Methods	19
5.1 SIB assembly	20
5.2 Electrochemical characterization	22
5.3 Hard carbon characterization using S/WAXS	23
6 Results and discussion	27
6.1 Electrochemical performance of half cells	28
6.1.1 Galvanostatic cycling of coin cells	28
6.1.2 Slope and plateau capacity contributions	29
6.1.3 Cyclic voltammetry and redox reactions	32
6.2 Hard carbon structural characterization	33
6.2.1 Measurement strategies for reproducibility	33
6.2.2 Scattering from HC electrodes	36
6.3 Inferred storage mechanisms from electrochemistry and scattering	39
6.4 Differences in the sodiation process	40

7 Conclusions and outlook	43
Bibliography	45
A Formation cycle of coin cells	I
B Voltage profiles of symmetric cells	III

List of Acronyms

Below is the list of acronyms that have been used throughout this thesis listed in alphabetical order:

CE	Counter electrode
CV	Cyclic Voltammetry
DMC	Dimethyl Carbonate
EC	Ethylene Carbonate
GIC	Graphite Intercalation Compound
HTT	Heat Treatment Temperature
HC	Hard Carbon
LIB	Lithium-Ion Battery
PVDF	Polyvinylidene Fluoride
PC	Polypropylene Carbonate
RE	Reference electrode
SIB	Sodium-Ion Battery
SEI	Solid Electrolyte Interphase
S/WAXS	Small- and Wide-Angle X-ray Scattering
WE	Working electrode
XRD	X-ray diffraction

List of Figures

2.1	A schematic overview of a SIB, including the main components of the electrochemical cell. The blue and orange arrows indicate in which direction the electrons and ions move during charge/discharge.	4
2.2	Schematic circuit diagram of a) a two-electrode cell and b) a three-electrode cell. Figure inspired by [16].	6
3.1	The hierarchical structure of HC. By zooming in on the HC particles, the porous structure is revealed, with pores highlighted in blue. Looking even closer at the structure, single sheets of graphene can be seen.	10
3.2	Different ways of visualizing the porosity of HC in a) 2D, and b) 3D.	11
3.3	3D schematic of the hard carbon structure with different storage sites represented by different colors. The green ions illustrate the pore filling mechanism while the blue ions have intercalated into a graphite-like domain of the structure, and the pink ions are adsorbed to surfaces and defects.	11
3.4	a) 2D illustration of the hard carbon structure with different storage sites, inspired by [30]. b) A typical charge curve for a SIB with hard carbon as anode material, featuring a sloping region and a plateau region.	12
3.5	Four proposed models of Na storage in hard carbon. The colors indicate how the storage mechanism varies along the voltage profile. Figure inspired by [30].	12
4.1	A typical setup for a S/WAXS experiment in transmission.	16
4.2	Typical scattering profile from S/WAXS measurements on HC. The curve can be divided into three different regimes which all yield information about the HC structure at different length scales.	17
5.1	HC electrode slurry coated on aluminium, with an electrode stamped out from the coating.	20
5.2	Schematic illustration of a HC/Na half cell.	21
5.3	Formation cycle and the second discharge of a HC/Na half cell cycled in configuration EC10. A large capacity fade is observed, likely due to SEI formation during the first discharge. Corresponding voltage profiles for cells cycled in EC5 and D10 can be found in Appendix A.	22

5.4	The sandwich cell used for ex situ scattering experiments on HC electrodes in S/WAXS. For transmission measurements the X-rays can pass through the windows in the center of the cell.	23
5.5	a) The inside of the vacuum chamber of the SAXS instrument. The radiation enters from the hole to the right and passes through a sample holder that is mounted to a moving stage in the middle of the figure. Transmitted X-rays are then collected by a detector located to the left of the figure. b) The sandwich cell holder with two sandwich cells mounted in it.	24
5.6	Ex situ SWAXS profiles of a sodiated HC where effects from air-exposure can be seen around $q = 0.06 \text{ \AA}^{-1}$. The vertical lines represent the upper and lower bounds of integration.	25
6.1	Voltage profiles of HC/Na half cells cycled in configuration a) EC5, b) EC10 and c) D10. The dots in a) - c) represent the stopping point of each curve where ex-situ S/WAXS measurements were performed. d) Voltage profile of a fully discharged cell in each of the three configuration.	29
6.2	Definition I of the slope-plateau boundary, established at $E_{\text{we}} = 0.1 \text{ V}$. The purple background represent the sloping region while the green side represent the plateau region.	30
6.3	The fraction of total capacity stemming from the slope versus plateau region in a) the first sodiation, b) the first desodiation and c) the second sodiation of HC, using definition I of the slope/plateau boundary. In the first sodiation/desodiation EC5 was cycled at C/10 and is therefore identical to EC10.	30
6.4	Definition II of the slope-plateau boundary, determined by the intersection of two tangent lines that follow the slope (blue tangent) and plateau (red tangent) respectively. The orange background represent the sloping region while the blue side represent the plateau region.	31
6.5	The fraction of total capacity stemming from the slope versus plateau region in a) the first sodiation, b) the first desodiation and c) the second sodiation of HC, using definition II of the slope/plateau boundary. In the first sodiation/desodiation EC5 was cycled at C/10 and is therefore identical to EC10.	31
6.6	Cyclic voltammograms of HC/Na half cells produced with a scanning rate of 0.1 mV s^{-1} . In a) the electrolyte was 1 M NaPF_6 in EC:PC and in b) the electrolyte was 1 M NaPF_6 in diglyme. In the inset of b), the values on the y-axis are the same as in a).	32
6.7	Ex situ SWAXS profiles of two pristine HC electrodes a) before normalization and b) after normalization at $q = 0.15 \text{ \AA}^{-1}$	33
6.8	Ex situ WAXS profiles of a pristine electrode and the HC powder used to synthesize the HC electrode slurry. The peak around $q = 1.5 \text{ \AA}^{-1}$ is attributed to the polymer binder used in the slurry mix.	34
6.9	Ex situ SWAXS profiles of a cycled HC electrode where one half of the electrode was washed and the other was not.	35

6.10	Ex situ SWAXS profiles of a sodiated HC electrode where one half of the electrode was exposed to air for 1 h. The inset shows an enlarged view of the high-q region where a peak emerging around $q = 2.1 \text{ \AA}^{-1}$ can be observed in the exposed sample.	35
6.11	S/WAXS profiles from ex situ measurements on HC electrodes used in galvanostatic cycling of coin cells in configuration a) EC5, b) EC10 and c) D10.	36
6.12	Scattering profiles in the microporous regime from ex situ measurements on HC electrodes used in galvanostatic cycling of coin cells in configuration a) EC5, b) EC10 and c) D10. All curves have been subtracted by the signal from a pristine HC electrode. Note that a potential exposure to trace amounts of H_2O lead to an increase in signal intensity around $q = 0.07 \text{ \AA}^{-1}$ for all samples in configuration D10, and the 91% sodiated sample in EC5.	37
6.13	Scattering profiles in the microporous regime from ex situ measurements on HC electrodes used in galvanostatic cycling of coin cells in configuration a) EC5, b) EC10 and c) D10. The integrated intensity of each curve (between $0.19 \text{ \AA}^{-1} < q < 0.5 \text{ \AA}^{-1}$) as a function of degree of sodiation are shown in the corresponding figure below a) - c). The colors in the background of figure d) - f) indicate where the voltage profile transitions from the sloping region (orange) to the plateau region (blue).	38
6.14	Lorentz-corrected WAXS profiles from ex situ measurements on HC electrodes used in galvanostatic cycling of coin cells in configuration a) EC5, b) EC10 and c) D10. The dashed vertical lines indicate the peak position of the pristine HC electrode.	39
A.1	Formation cycle and the second discharge of a HC/Na half cell cycled in configuration EC10. A large capacity fade is observed, likely due to SEI formation during the first discharge.	I
A.2	Formation cycle and the second discharge of a HC/Na half cell cycled in configuration EC5. A large capacity fade is observed, likely due to SEI formation during the first discharge.	I
A.3	Formation cycle and the second discharge of a HC/Na half cell cycled in configuration D10. A large capacity fade is observed, likely due to SEI formation during the first discharge.	II
B.1	Voltage profile of symmetric Na/Na cells cycled at 0.07 mA cm^{-2} , 0.14 mA cm^{-2} and 0.7 mA cm^{-2} , corresponding to charge rates of C/10, C/5 and 1C in the HC/Na half cells.	III

List of Figures

List of Tables

5.1 An overview of the charge rates and electrolyte solvents used in the different cell cycling configurations. Apart from these differences, the cell chemistry is identical in the different configurations.	21
--	----

List of Tables

1

Introduction

The development and subsequent commercialization of rechargeable alkali metal-ion batteries, in particular the lithium-ion battery (LIB), can be regarded as one of the greatest achievements in recent human history [1]. As batteries get smaller and lighter, consumer electronics become more portable, and today almost everyone owns a device that uses a LIB for energy storage. At the same time, the LIB has played a major role in the blossoming of the electric vehicle industry, and continues to find new applications in areas such as aviation, power tools and grid based electric energy storage systems [1]. However, the growing number of applications has lead to a high demand for the raw materials used in LIBs. As a consequence, metals like cobalt and lithium (Li) are becoming increasingly expensive [2] and the scarcity of materials can become a bottleneck in the production of new batteries. This has prompted researchers to develop batteries that use cheaper and more abundant raw materials such as sodium (Na), aluminium (Al), potassium (K) and magnesium (Mg).

An alkali metal-ion battery that benefit from operating under the same working principles as the LIB is the sodium-ion battery (SIB) [2]. The possibility of using Na-ions as charge carriers in batteries was demonstrated already in 1980 [3], but research on SIBs only truly took off around 2010 [4], and the technology is just now starting to become commercialized. Li has a significantly higher gravimetric and volumetric energy density than Na [4], and thus the obvious technology to invest in back then was the LIB. There are nevertheless advantages of using Na over Li in batteries. Li make up only 0.002 % of the Earth's crust and is produced mainly in South America and Australia, while Na make up approximately 2.3 %, making it a 1000 times more abundant resource [4]. A reduced risk of supply chain issues therefore poses the SIB as a potentially low cost and environmentally friendly alternative to the LIB [5].

Despite its similarities, manufacturing a SIB is not as simple as replacing the Li with Na. Most LIBs today use graphite as anode material, but Na can not intercalate effectively in graphite. This has lead researchers to look into other materials to use in the anode of SIBs. One alternative is hard carbon (HC), a non-graphitizable form of carbon synthesized from carbon-rich precursors such as lignin and sucrose [6]. As such, the material can be produced both sustainably and at a low cost by using e.g. industrial bio-waste [7]–[10]. Moreover, HC show excellent performance in its cycling stability and storage capacity, making it the anode material of choice in SIBs today [2].

1. Introduction

Nevertheless, uncertainties remain regarding precisely how Na-ions are stored in HC during battery operation, mainly due to the complex amorphous structure of the material. The precise nanostructure is highly correlated to the HC fabrication process (pyrolysis temperature and precursor material), leading to inconsistencies when researchers compare results obtained from vastly dissimilar systems. For this reason a more common approach today is to view hard carbon as a class of materials rather than a single type of material.

To understand the storage mechanism a technique that can characterize the bulk nanostructure of HC electrodes is needed. A method that is well suited for analyzing materials lacking long-range order is small- and wide-angle X-ray scattering (S/WAXS) [11]. It is a non-destructive technique [12] that can be used to study structures from Å up to mm length scales [11], and has previously been employed to study the sodiation process in HC [13], [14].

While previous works have compared the storage mechanisms in HCs synthesized from a variety of precursors or heat treatment temperatures, there is a gap in the literature regarding how other parameters such as the electrolyte and charge rate might affect the Na-ion storage. It is possible that electrolytes forming different solid electrolyte interphases (SEIs) or solvation shells would influence the Na-ion kinetics. As for the effects of different charge rates, a slower charge rate could lead to Na-ions being able to diffuse further into the HC structure, leading to less Na plating and better usage of the bulk HC volume.

As we look towards the future, a better understanding of the sodiation process in HC along with strategies to enhance the sodiation will allow for easier and more sophisticated design of high performance SIBs in the future. This masters thesis aims at contributing to this endeavor. More specifically, the work will (i) investigate the sodiation process in HC electrodes by correlating the results from S/WAXS experiments and electrochemical methods and, (ii) identify in the storage behavior when using different electrolytes and charge rates and, (iii) discuss the origins of possible differences arising when the electrolyte and charge rate is varied.

2

Batteries

Batteries can store electrical energy in the form of chemical energy, and are therefore a type of electrochemical storage system. Rechargeable batteries have become a staple among the different energy storage systems in the world today. By their nature, these batteries are complex systems with many interacting parts working together. In this chapter the basic working principles and main cell components that make up a rechargeable battery will be presented using the SIB as the foundation.

2.1 The electrochemical cell

The first electric battery was built in 1800 by Alessandro Volta [15]. This so called "voltaic pile" consisted of alternating disks of zinc and silver, separated by a cloth drenched in a sodium chloride solution. Soon it was realized that this electrochemical device could function as an energy storage system, and since then, countless electrochemical systems (such as the zinc-manganese oxide cell and the rechargeable lead-acid battery to name a few) have been developed [15]. Fast forward to today, the battery technology that has conquered the market is the rechargeable lithium-ion battery.

An electrochemical cell is by definition a device that generates electrical energy from spontaneous chemical reactions (known as a Galvanic cell), or utilizes electrical energy to drive chemical reactions (electrolytic cell). The main components of an electrochemical cell are the two electrodes (anode and cathode) and the electrolyte (see fig. 2.1). A separator is often submerged in the electrolyte to prevent contact between the electrodes, which would otherwise lead to short circuiting of the cell. The electrodes are placed on current collectors that aid in conducting electrons to an external circuit.

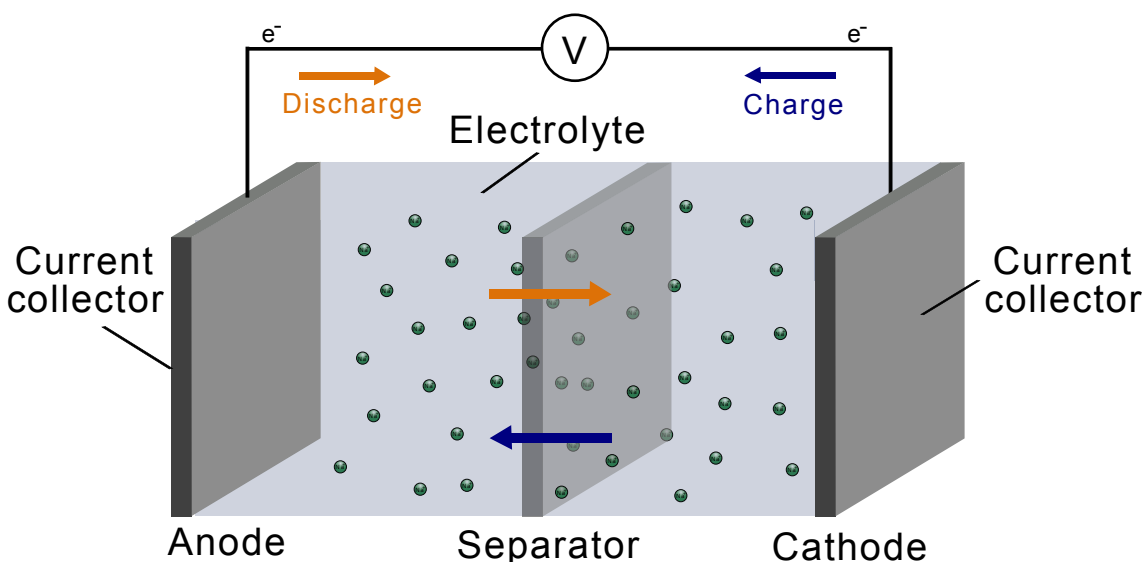


Figure 2.1: A schematic overview of a SIB, including the main components of the electrochemical cell. The blue and orange arrows indicate in which direction the electrons and ions move during charge/discharge.

In an oxidation reaction, an atom or molecule loses an electron, while an electron is gained by a chemical species in a reduction reaction. These are known as redox (reduction–oxidation) reactions and play a crucial role in batteries. When a voltage is applied over the two electrodes in a cell, oxidation takes place at the positive electrode while reduction occurs at the negative electrode. In this scenario, the electrochemical cell is said to be charging. When the cell is instead being discharged, reduction takes place at the positive electrode and oxidation occurs at the negative

electrode. In battery research, the negative electrode is referred to as the anode by convention, while the positive electrode is known as the cathode. Note that this is contrary to the convention used in electrochemistry, where the anode is defined as the electrode at which oxidation occurs and the cathode is the electrode hosting reduction reactions.

The SIB is sometimes called a "rocking-chair battery". The name comes from the idea that Na-ions are being transported back and forth between the electrodes when the battery is being charged/discharged. This phenomenon is integral to the SIB, since redox active species (i.e. atoms or molecules that can change their valency) are needed for the redox reactions to take place at the electrodes. During charge, the Na-ions acts as the redox active species by undergoing oxidation and releasing electrons at the cathode. They subsequently move through the electrolyte and recombine with the electrons (that are transported via an external circuit) at the anode by undergoing reduction. Naturally, the ions and electrons move in the opposite direction when the cell is instead being discharged.

The cell voltage of an electrochemical cell is defined as the difference between the electrode potentials, i.e.

$$E_{\text{cell}} = E_{\text{C}} - E_{\text{A}} \quad (2.1)$$

where E_{cell} is the cell potential, E_{C} is the cathode potential, and E_{A} is the anode potential. However, the individual potentials of each electrode can not be measured, only the difference between the two. Therefore an arbitrary zero potential needs to be chosen, which is why the standard electrode potential, E° , of the hydrogen electrode redox couple $2\text{H}_{(\text{aq})}^{+} + 2\text{e}^{-} \rightleftharpoons \text{H}_{(\text{g})}$ is defined as $E^{\circ} = 0$. In this way, the potential difference between two electrodes is always measured in relation to this reference level.

Nevertheless, in many cases when investigating a particular electrode material, only one of the two electrode potentials is of interest. In this scenario the ideal configuration is the so called "three-electrode cell" (see fig. 2.2) in which the potential difference between a working electrode (the electrode of interest, WE) and a reference electrode (RE) is measured. When no current is flowing through the RE, the potential of only the WE can be monitored. When instead a "two-electrode setup" is used, the counter electrode (CE) simultaneously acts as a RE. In this setup the WE potential can not always be monitored if the potential of the CE is affected by the current running through the circuit.

The "half-cell setup" is a type of two-electrode configuration in which the WE is coupled to a metallic electrode functioning as both CE and RE simultaneously. This setup is commonly employed in research today because of its simpler configuration compared to the three-electrode setup. When relatively low currents are used, polarization of the CE can be avoided and the WE potential can be estimated.

An important metric when discussing batteries is capacity. Often measured in units

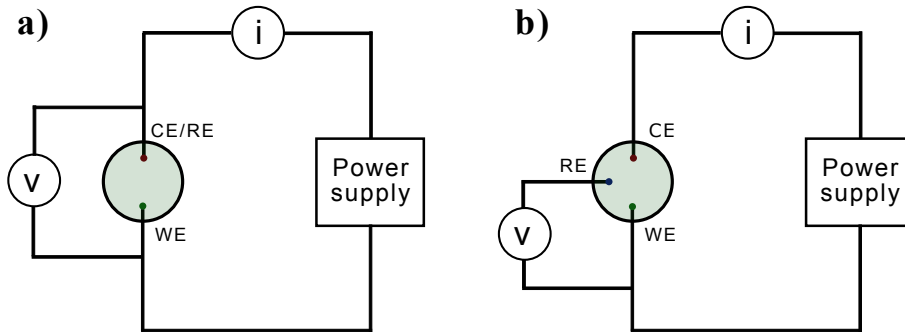


Figure 2.2: Schematic circuit diagram of a) a two-electrode cell and b) a three-electrode cell. Figure inspired by [16].

of mA h or Wh, the capacity yields a measure of how many charge carriers can be stored in a given cell or electrode. When the capacity of the anode and cathode are different from one another, the electrode with the lowest capacity will limit the cell capacity. In research, the capacity per weight can sometimes be more relevant since this may yield a more fair measure of how well suited a material is for certain applications. This metric is known as specific capacity and is usually presented in units of mA h g^{-1} .

Another term that often appears in the battery community, and is highly relevant for this thesis is "charge rate". When a battery is charged to its maximum capacity in 1 h (from being fully discharged), it is said to have been cycled using a charge rate of 1C. Conversely, if a battery is entirely charged in ten hours, the charge rate is C/10.

2.2 Electrochemical characterization techniques

Galvanostatic cycling with potential limitation (GCPL) is a commonly employed method to test the performance of batteries. By connecting a cell to a potentiostat, either the voltage or current can be controlled in order to charge or discharge the cell. In addition, the electrical response of the cell can be monitored with the potentiostat, and importantly the voltage of the WE can be measured with respect to a RE. Therefore, a typical cell cycling protocol involves letting a constant current run through the circuit until a predefined voltage limit is reached, at which point the charging or discharging is terminated. In a software included with most potentiostats, scripts can be put together so that multiple charges and discharges of a cell can be implemented, thereby simulating scenarios in real-world applications.

Cyclic voltammetry (CV) is a technique used for studying redox reactions taking place at the electrodes of batteries. During measurements, a voltage is applied over the cell while the current response of the cell is recorded. Unlike galvanostatic cycling, the potential is swept linearly back and forth between an initial and final value.

2.3 Anode materials in SIBs

In the context of batteries, the active material of an electrode is the material that facilitates the redox reactions, and usually make up around 80 % - 95 % of the total mass of the electrode. Because of its functionality in the cell, the most important properties of the active material is its electric and ionic conductivity, its stability against the electrolyte and its capability of storing ions inside the material. Other materials are also present in the electrode to enhance the electric conductivity and bind the constituents together, but are only present in smaller amounts. Thus, when discussing "electrode materials" for LIBs or SIBs, what is often implied is the active material in the electrode.

Graphite has long been the predominant anode material in LIBs thanks to its availability, high gravimetric and volumetric capacity and low cost [4], [17]–[19]. Unfortunately, Na can not intercalate effectively in graphite. This is not simply because Na has a larger atomic radius than Li, since larger alkali metals such as potassium can form stable graphite intercalation compounds (GICs) [20], [21]. It is rather the thermodynamics of the system that determines which GICs become energetically favorable, as shown by density functional theory calculations on different alkali metal-GICs [22]. By separating the GIC formation energy contributions into the binding energy and the energy required for structural deformation of the graphite as a result of intercalation, it was found that the structural deformation energy increases linearly with the radius of the alkali metal-ion, while the binding energy is largest for Na. For this reason, intercalation of Na atoms into graphite is always thermodynamically unfavorable compared to its other alkali metal counterparts [22].

As a consequence of graphite not being a viable choice of material to facilitate sodium storage, alternative anodes for SIBs have been heavily researched in recent years [23]. Some of these include metals, alloys, carbonaceous materials, oxides and polyanionic compounds [4]. This thesis is focused on studying hard carbon which is part the of the carbonaceous class of materials.

2.4 Electrolytes in SIBs

The electrolyte serves as a pathway for Na-ions to be transported between the electrodes in a SIB. A well performing electrolyte is crucial for any successful battery, and some important properties to optimize for include its thermal and electrochemical stability window, ionic conductivity, cost, toxicity and environmental friendliness [24]. Electrolytes in SIBs constitute of sodium salts dissolved in a solvent solution, sometimes together with additional additives.

Many different electrolytes have been developed over the years, and can be divided into five categories: organic electrolytes, ionic liquids, aqueous electrolytes, inorganic solid electrolytes and solid polymer electrolytes [24]. Organic electrolytes are the most popular in SIBs today thanks to their adequate ionic conductivity combined

2. Batteries

with their compatibility with many electrode materials and separators [24]. Two organic electrolytes are under investigation in this project, both using NaPF₆ as the salt, but with either ethylene carbonate:propylene carbonate (EC:PC) or diethylene glycol dimethyl ether (diglyme) as solvent. The former is known as an ester-based type of electrolyte, while the latter is an ether-based electrolyte. These were chosen

EC:PC-based electrolytes have shown commendable properties in previous studies [25], with EC being a popular solvent due to its high dielectric constant leading to favorable salt dissolution [24]. It is also believed to aid the formation of stable interphases on the electrode because of the strong interaction with anions in the electrolyte [24]. Although PC has a lower dielectric constant and can contribute to cell degradation, it is often used together with EC to improve the liquid temperature range of the electrolyte [24].

Electrolytes with diglyme-based solvents have been used to successfully cointercalate Na in graphite by forming a ternary GIC with the solvation shell and the carbon [26]–[29]. It is currently unclear how compatible this type of electrolyte is with HC, but a compelling possibility is that more intercalation into graphite-like domains of the HC electrode could be enabled when using diglyme as the electrolyte solvent.

When it comes to the salt used in electrolytes for SIBs, NaPF₆ is a favorable option. Not only is it considered the most promising alternative for practical applications, but it is also less explosive and more compatible with aluminium than e.g. NaClO₄, NaTFSI or NaFSI [24].

3

Hard carbon

Up to date, hard carbon is the most popular anode material in SIBs on account of its high storage capacity and cycling stability. In addition the material can be produced cheaply from renewable, carbon-rich biomass precursors, which is advisable for large-scale production and successful commercialization of SIBs. The microstructure is nevertheless characterized by disorder and complexity and is heavily dependent on the precursor. In this chapter, the structure of the material is elaborated, along with an account of the different Na storage mechanisms that may be present when using HC electrodes in SIBs.

3.1 Structure and synthesis

The fundamental building block of the HC structure is graphene, i.e. carbon atoms arranged in a hexagonal lattice. When layers of graphene stack and are held together by van der Waals forces, they form graphite. This stacking of graphene layers can be synthesized in a complex process involving carbonization, where one of the fundamental steps is to heat-treat carbon-rich materials such as hydrocarbons or other organic compounds to around 3000 °C. Hard carbon however, is characterized by the property that it does not form graphite even when being heated to these temperatures [2]. Instead the twisted and tangled graphene sheets are retained in hard carbon when undergoing heat treatment, leading to the presence of pores (see fig. 3.1 and 3.2). Despite the generally disordered structure, some of the graphene sheets may still end up stacking with each other, meaning that there are instances of graphite-like domains in the material. Furthermore, the graphene lattice can feature defects such as vacancies and heteroatoms, and the homogeneity can be disrupted by heptagons and pentagons [30].

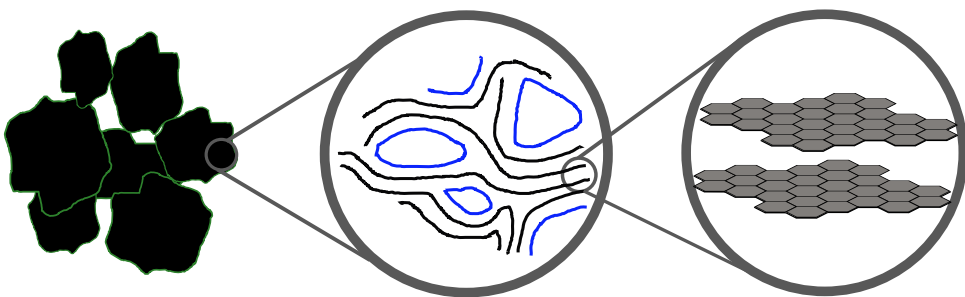


Figure 3.1: The hierarchical structure of HC. By zooming in on the HC particles, the porous structure is revealed, with pores highlighted in blue. Looking even closer at the structure, single sheets of graphene can be seen.

In literature, the terms "closed pore" and "open pore" are sometimes used to distinguish between voids inside the bulk of the material and pores connected to the surface of HC particles. Furthermore, the structure of HC is often visualized in 2D, since the porosity is more easily highlighted in this picture. This depiction can nevertheless not always mediate the full complexity of the material, and albeit convoluted, a 3D overview of the structure can be seen in figure 3.2.

The lack of long range order and crystallinity make hard carbon difficult to classify, as the microstructure can vary from sample to sample. This is because the structure is heavily dependent on the manufacturing process. Hard carbon is frequently fabricated from precursors with a predominantly cross-linked structure, and it is believed that the crosslinking plays a role in preventing graphite formation [2]. In addition, the morphology of the precursor is preserved to a high degree, making it a crucial factor to consider when designing the material. Other than the choice of

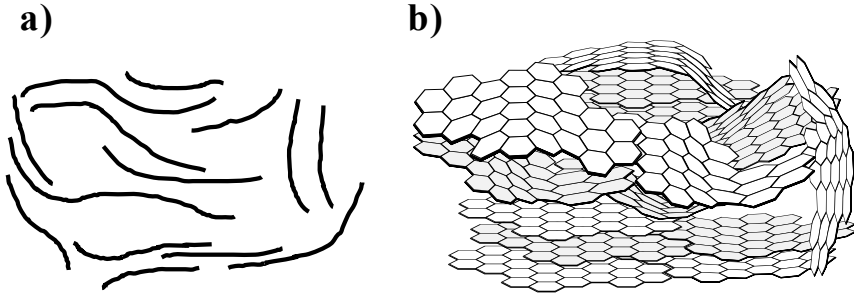


Figure 3.2: Different ways of visualizing the porosity of HC in a) 2D, and b) 3D.

precursor, the heat treatment temperature also affect the resulting structure, where an increasing temperature generally decreases the volume of open pores, while the volume fraction of pores in the bulk increases [2], [31]. Similarly, the mean radius of closed pores increases with heat treatment temperature [14]. All of these factors will inevitably affect the storage of Na-ions in the material.

3.2 Sodium storage mechanisms in hard carbon

The process of inserting Na-ions into hard carbon is called the sodiation process. Over the years, several models have been proposed to explain the sodiation in hard carbon [30]. Despite the efforts, there is still no consensus on the topic, leading researchers to interpret similar results in vastly different ways. The three most common storage mechanisms that appear in popular models describing the sodiation process are (1) Na filling in pores (2) intercalation between graphene sheets and, (3) adsorption of Na on defect sites and surfaces. A schematic representation of the mechanisms can be seen in figure 3.3. Different features of the structure are responsible for the different mechanisms, as can be seen in figure 3.4a) as well. For example, increasing the number of closed pores would affect the pore filling mechanism, while introducing more defects in the material should lead to more defect adsorption [30]. In order to rationally design a hard carbon anode for usage in SIBs it is thus important to understand what underlying processes contribute to the experimental observations.

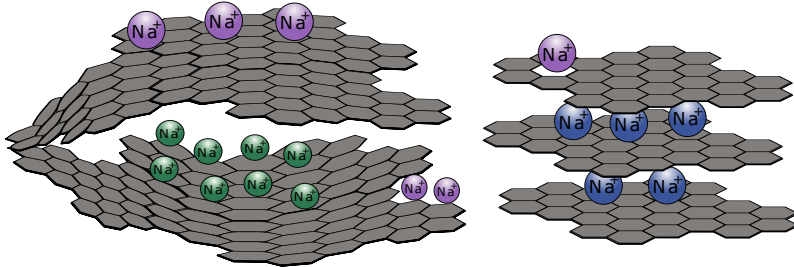


Figure 3.3: 3D schematic of the hard carbon structure with different storage sites represented by different colors. The green ions illustrate the pore filling mechanism while the blue ions have intercalated into a graphite-like domain of the structure, and the pink ions are adsorbed to surfaces and defects.

3. Hard carbon

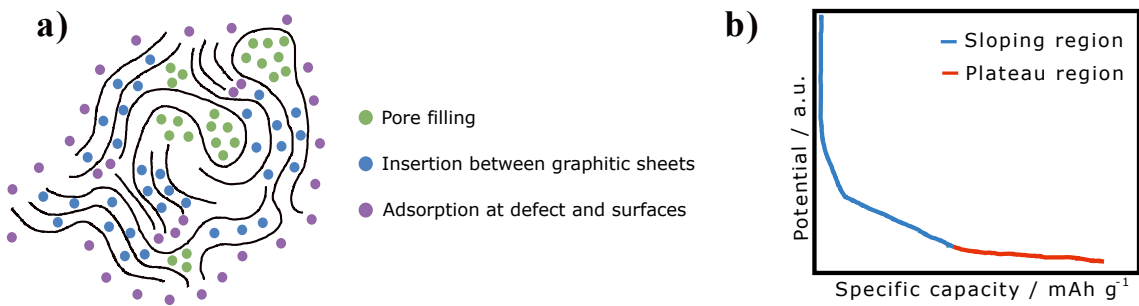


Figure 3.4: a) 2D illustration of the hard carbon structure with different storage sites, inspired by [30]. b) A typical charge curve for a SIB with hard carbon as anode material, featuring a sloping region and a plateau region.

A typical SIB voltage profile is shown in fig. 3.4b). The curve is usually divided in to a high-potential sloping region and low-potential plateau region. A persisting matter of controversy in research is when scientists attribute different storage mechanism to these two regions of the curve. A summary of the most popular models are presented in figure 3.5, and it is clear from the figure that the they all contradict one another.

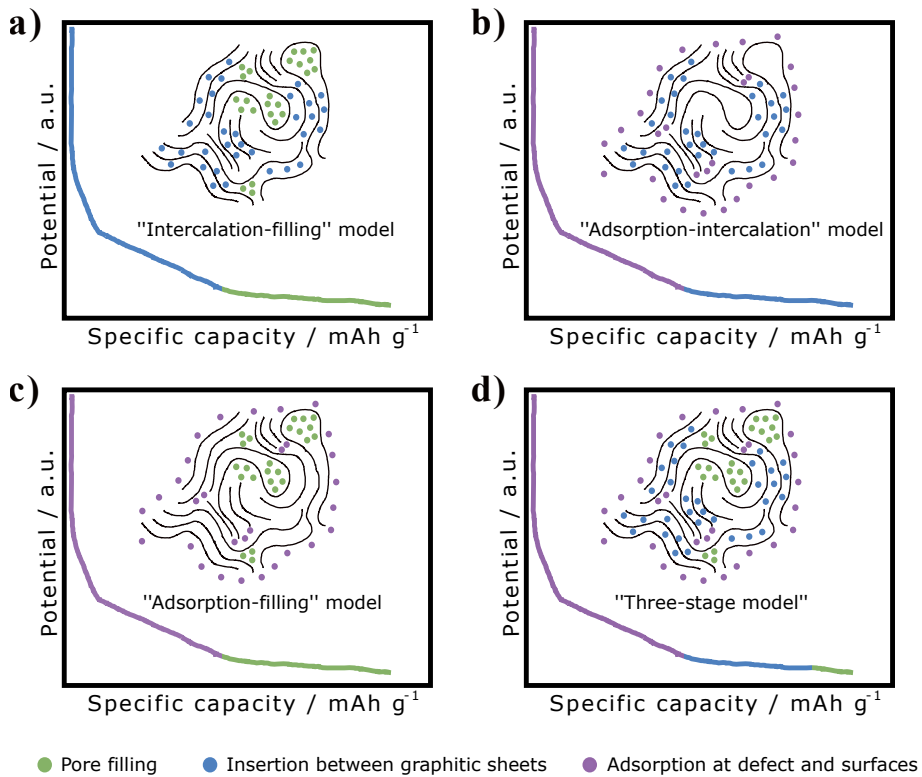


Figure 3.5: Four proposed models of Na storage in hard carbon. The colors indicate how the storage mechanism varies along the voltage profile. Figure inspired by [30].

In 2000, Stevens and Dahn [32] studied the insertion of Na into hard carbon anodes synthesized from glucose samples. They concluded that the sloping region of the potential could be attributed to Na intercalation between parallel layers, and reasoned that as the insertion increased, the potential for further intercalation decreased. Furthermore they attributed the plateau region with Na filling in pores. They claimed that for these sites the chemical potential was close to that of Na, which would be the reason for the low voltage in the plateau region. In a follow-up paper the authors further confirmed their results by conducting *in situ* XRD and SAXS experiments [33]. In this manner they could observe an increase in interlayer spacing at the sloping region, which would be explained by intercalation of Na in the graphite-like domains. At the same time the results from the SAXS experiments showed that the electron density in the pores remained unchanged during the sloping region, but changed along the plateau region, implying that Na-ions filled the pores in the hard carbon only along the plateau region [33].

In contrast to this, Zhang et al. [34] studied the storage behavior in carbon nanofibers synthesized from polyacrylonitrile polymers. By preparing samples at various heat treatment temperatures, they found that the sloping region of the voltage profile disappeared when the graphene layers became parallel with small interlayer spacing, implying that the sloping region was a result of Na-ions adsorbing on isolated graphene sheets rather than from intercalation. In addition they did not observe any increase in interlayer spacing from XRD measurements compared to Stevens and Dahn. Moreover, they found that the capacity of the plateau region became prominent for samples containing larger amounts of pores, suggesting that Na filling was the responsible mechanism in this region.

3. Hard carbon

4

S/WAXS analysis

The SAXS instrument is a powerful tool for studying structures that lack long-range order. Another advantage of the instrument is that the signal produced from a S/WAXS measurement contains information about the structure on Å up to micrometer length scale. Considering that HC is a material with both a hierarchical and amorphous structure, the SAXS instrument is therefore well suited for investigating the sodiation process in HC.

4.1 Basic principles of S/WAXS

S/WAXS are non-destructive X-ray scattering techniques that can provide information about the structure of a material on the Å to millimeter length scale. In S/WAXS, the momentum transfer vector \vec{q} is defined as the difference between the incoming and the scattered wave vector, $\vec{q} = \vec{k}_0 - \vec{k}_1$ (see fig. 4.1), and the momentum transfer $q = |\vec{q}|$ can be calculated as

$$q = \frac{4\pi \sin \theta}{\lambda} \quad (4.1)$$

where λ is the wavelength of the X-ray source and 2θ is the angle of the scattered X-rays. Together with the Bragg condition $n\lambda = 2d \sin \theta$ it is possible to rewrite equation 4.1 as

$$d = \frac{2\pi}{q}. \quad (4.2)$$

where d is a characteristic distance in a periodically repeating structure, such as the distance between atomic planes in a crystal. The same relation can be used to approximate the size of features lacking long range order in a S/WAXS experiment.

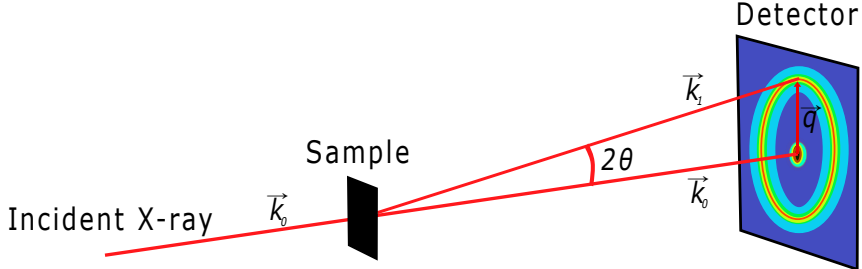


Figure 4.1: A typical setup for a S/WAXS experiment in transmission.

From equation 4.2 we see that larger q -values correspond to smaller features, and vice versa. Thus different curves can be fit to the SAXS scattering data to describe different structural features. When the angle of the scattered X-rays become sufficiently large, the technique is instead referred to as WAXS. In this mode, smaller features such as distances between crystal planes can be inferred.

During an experiment, a detector measures the intensity of the scattered light, and the resulting 2D-interference pattern is characteristic of the internal structure of the sample [12]. The resulting scattering data is often presented as radially integrated intensity as a function of q (see figure 4.2). In SAXS the scattering depends on variations in the electron density distribution rather than from single atoms as in X-ray diffraction. This means that both particles in a solution as well as voids/pores in a matrix can be detected using SAXS as long as there is a measurable contrast in electron density between the particles/pores and the surrounding matrix.

The scattering intensity that arrives at the detector can be described by the equation

$$I(q) = (\rho_p - \rho_m)^2 N_p V_p^2 P(q) S(q) \quad (4.3)$$

where $\rho_p - \rho_m$ is the contrast in scattering length density between particle (or pore) and matrix, N_p is the number of particles, V_p is the volume of particles, $P(q)$ is the "formfactor" that relates to the intra-particle interference (shape and size of particles) and $S(q)$ is the "structure factor" that relates to the inter-particle interference (spacing and interactions between particles).

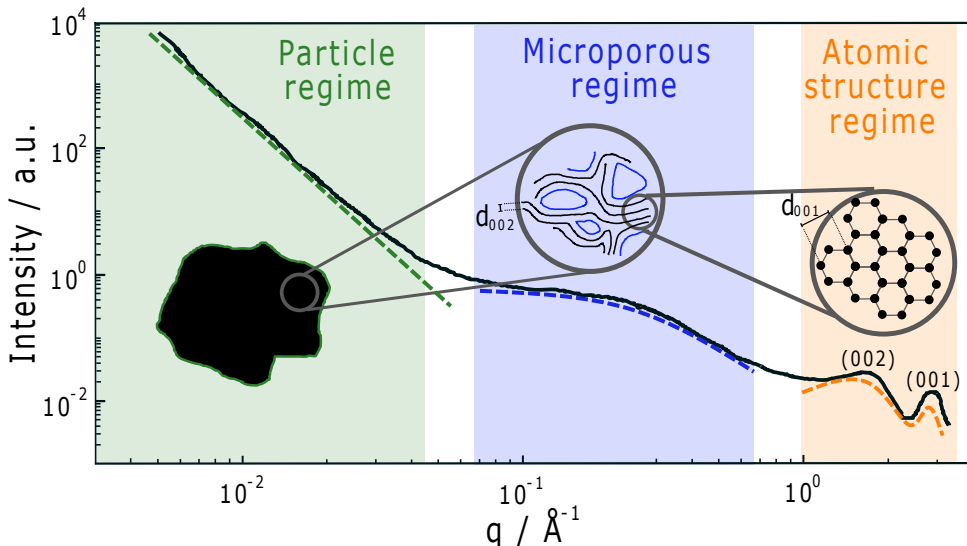


Figure 4.2: Typical scattering profile from S/WAXS measurements on HC. The curve can be divided into three different regimes which all yield information about the HC structure at different length scales.

4.2 Studying hard carbon sodiation with S/WAXS

The scattering profile from hard carbon can be divided into three different regimes which yield information about the structure at different length scales (see fig. 4.2). In the low-q regime, a decreasing slope from the surface of the micron-sized particles are found. In the intermediate region, a "shoulder" appears due to the electron density difference between the micropores and the carbon matrix. In the high-q regime a broad diffraction peak emerges as a result of the stacked graphene sheets.

When Na-ions are inserted into HC, the structure of the electrode changes, and consequently the S/WAXS curve is affected. The changes that arise in the different regimes of the curve can therefore be related to the sodiation process. If Na-ions start filling the micropores there will be a decreased contrast between the previously empty pores and the carbon matrix, which leads to a decreasing intensity in the microporous regime. The peaks visible in the atomic structure regime come from the graphite-like domains. The first diffraction peak (002-peak) can be related to the interlayer distance between graphene sheets. If Na-ions intercalate between the sheets, the (002)-peak is expected to shift to lower q because of an increasing interlayer spacing. A broad peak around 2.1 Å have previously been identified after extensive pore filling from densely packed Na within micropores [13]. In the particle

4. S/WAXS analysis

regime, the slope can be affected by changes in surface roughness and the intensity is related to the specific surface area of particles. SEI formation could therefore affect the curve in this regime, while the sodiation process itself is not expected to heavily influence the scattering intensity in this q-range.

5

Methods

The experimental work of the project is presented in this chapter. This includes details about the SIB assembly, electrochemical methods used, as well as the X-ray scattering experiments.

5.1 SIB assembly

HC electrodes were prepared by mixing a slurry consisting of 85 wt% HC (CARBOTRON P, Kureha Battery Materials Japan), 5 wt% carbon additive (Carbon black Super P®, ThermoFisher) and 10 wt% polyvinylidene fluoride binder (PVDF, Sigma Aldrich). N-methylpyrrolidone (Sigma Aldrich) was used as solvent, and after 2-3 h of magnetic mixing the slurry was coated onto a current collector made of aluminium (see fig. 5.1). The coated electrode was put under vacuum for about 12 h at 120 °C to evaporate the toxic solvent. A 10 mm puncher was used to stamp out the final HC electrodes, which were then vacuum dried a second time at 120 °C for 12 h. Finally, the electrodes were transferred to an argon-filled glove box for storage.



Figure 5.1: HC electrode slurry coated on aluminium, with an electrode stamped out from the coating.

An electrolyte consisting of 1 M NaPF₆ (Sigma Aldrich) in diglyme (Sigma Aldrich) was prepared by first drying molecular sieves (3 Å, Thermo Scientific) in vacuum at 220 °C for 24 h. To remove any trace of H₂O from the diglyme, the solvent was then put in a beaker together with the dried sieves for a few days. Meanwhile, the salt was dried at 80 °C for 24 h. Using a filter to avoid contamination from the sieves, the solvent was finally mixed with the salt to the desired fraction of 1 M NaPF₆ in the electrolyte.

All coin cells used for studying the sodiation process in HC were half cells consisting of HC (10 mm Ø) as the WE, metallic sodium (11 mm Ø, dry stick, Thermo scientific chemicals) as CE and a glass microfiber filter as separator (16 mm Ø, Whatman GF/C). Two different electrolytes were used, namely 1 M NaPF₆ in EC:PC (50:50 by wt., E-Lyte Innovations) and 1 M NaPF₆ in diglyme (prepared on-site). The coin cells were assembled in an argon-filled glove box to minimize contamination

and unwanted reactions such as oxidation. The constituents of a coin cell can be seen in figure 5.2. The cells were assembled by stacking the parts on top of each other, and then sealed by clamping the cap to the gasket. Furthermore, the cell pressure was controlled by the spring and spacer.

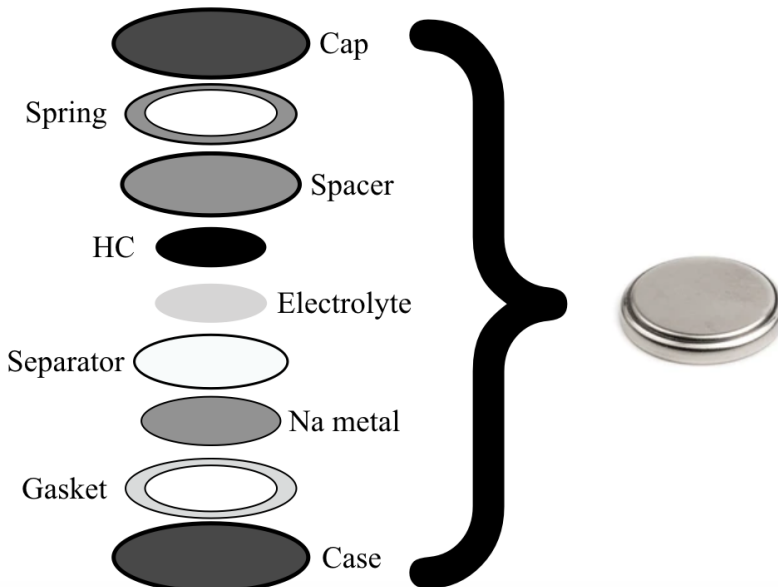


Figure 5.2: Schematic illustration of a HC/Na half cell.

Three coin cell configurations were used to investigate changes in storage mechanisms for different charge rates and electrolytes. The baseline configuration (EC10, see table 5.1) consisted of HC/Na half cells cycled at C/10, with EC:PC (1:1 wt%) as the electrolyte solvent. The second configuration (EC5) uses the same electrolyte as EC10 but is cycled at C/5, while the third configuration (D10) uses diglyme instead of EC:PC as electrolyte solvent, while being cycled at C/10.

Table 5.1: An overview of the charge rates and electrolyte solvents used in the different cell cycling configurations. Apart from these differences, the cell chemistry is identical in the different configurations.

Configuration name	Charge rate	Electrolyte solvent
EC10	C/10	EC:PC (1:1 wt%)
EC5	C/5	EC:PC (1:1 wt%)
D10	C/10	Diglyme

5.2 Electrochemical characterization

All GCPL experiments in this project were performed using a multichannel potentiostat (580 Battery Test System, Scribner). The HC/Na half cells were assembled such that the resting potential of the HC electrode was higher than that of the Na-metal CE. This meant that to sodiate the HC electrode, the cell was first discharged. Likewise when the cell was charged, the HC electrode was desodiated.

The cells were first cycled with a SEI formation protocol consisting of one full discharge/charge cycle at a constant current corresponding to a charge rate of C/10. The potential limits were 0.02 V and 2 V for the discharge and charge respectively. These parameters were used in the first charge/discharge of all cells cycled in the three configurations described in table 5.1. After the formation cycle, the HC/Na half cells were sodiated a second time (see fig. 5.3). By varying the cut-off voltage, the cells were stopped at different degrees of sodiation. In each configuration, three cells were terminated in the sloping region, and three in the plateau region.

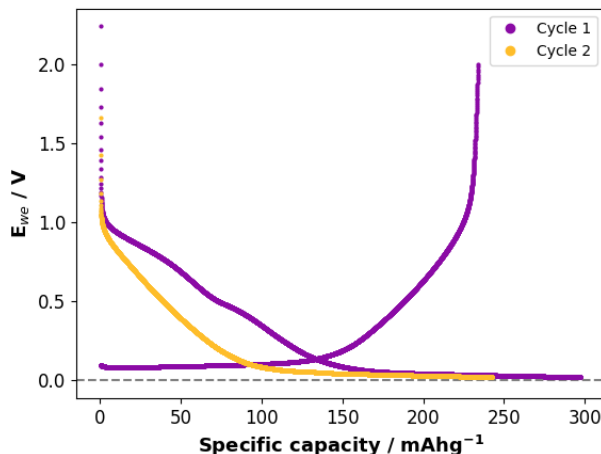


Figure 5.3: Formation cycle and the second discharge of a HC/Na half cell cycled in configuration EC10. A large capacity fade is observed, likely due to SEI formation during the first discharge. Corresponding voltage profiles for cells cycled in EC5 and D10 can be found in Appendix A.

Galvanostatic cycling experiments were performed on Na/Na symmetric cells using 1 M NaPF₆ in EC:PC (1:1 by wt.) as electrolyte. Two measurements were performed, one in which a current corresponding to a charge rate of 1C was used, and one where a charge rate of C/10 was used in the first few cycles followed by charge rate of C/5 in subsequent cycles. Rather than having a potential limitation, each charge/discharge was terminated after 1 h. The results from these experiments can be viewed in Appendix B.

CV experiments were performed using a multichannel potentiostat (VMP3, Bio-Logic), and a linear sweep of 0.1 mV s^{-1} was used between 0 V to 2 V. Two voltammograms of HC/Na half cells were recorded, one for each of the two electrolytes used in this study.

5.3 Hard carbon characterization using S/WAXS

Cycled HC electrodes were extracted from the HC/Na coin cells inside an argon filled glove box. The electrodes were subsequently washed and dried before being placed in a sample holder (see figure 5.4) for S/WAXS measurements. The electrodes were clamped between two Kapton tape films, separated by an O-ring, and the sample holders were held together by six screws.

For the washing procedure, solvents were first dried using molecular sieves (3 \AA , Thermo Scientific, dried in vacuum at 220°C for 24 h) to remove potential traces of H_2O . For the cells in configuration EC5 and EC10, dimethyl carbonate (DMC) was used, while diglyme was used for the cells in configuration D10. The electrodes were submerged for 60 s in a beaker filled with solvent. This method was chosen based on results from a previous study where different washing procedures were investigated [35]. In addition, no electrodes were submerged in the same beaker, and all beakers were dried in vacuum for 8 h in 120°C to reduce the risk of H_2O contamination. After washing, the electrodes were left to dry for a few minutes.

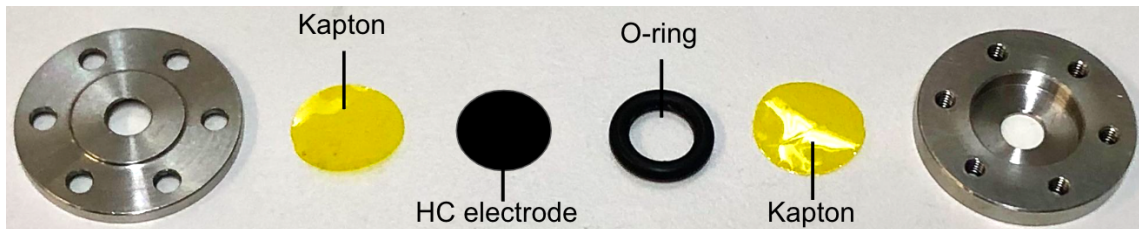


Figure 5.4: The sandwich cell used for ex situ scattering experiments on HC electrodes in S/WAXS. For transmission measurements the X-rays can pass through the windows in the center of the cell.

S/WAXS measurements on HC electrodes were performed using a MAT:Nordic X-ray scattering instrument (SAXSLAB). The instrument was equipped with a high brilliance Rigaku 003 X-ray micro-focus, a Cu- $\text{K}\alpha$ radiation source with a wavelength of $\lambda = 1.5406 \text{ \AA}$ and a Pilatus 300 K detector system. Ex situ cells were mounted on a sample holder and placed inside a vacuum chamber (see fig. 5.5). Two measurements were performed on each sample, one in a SAXS configuration where the sample-to-detector distance was 1080 mm and an exposure time of 1000 s was used, and one in a WAXS configuration using a sample-to-detector distance of 134 mm and a 600 s exposure time. In the SAXS configuration, intensities could be obtained for q -values ranging between 0.005 \AA^{-1} - 0.3 \AA^{-1} , while in WAXS the

5. Methods

q -range was 0.07 \AA^{-1} - 2.1 \AA^{-1} . The instrument was calibrated using lanthanum hexaboride. The 2D scattering patterns collected by the detector were radially integrated before being further analyzed and post-processed.

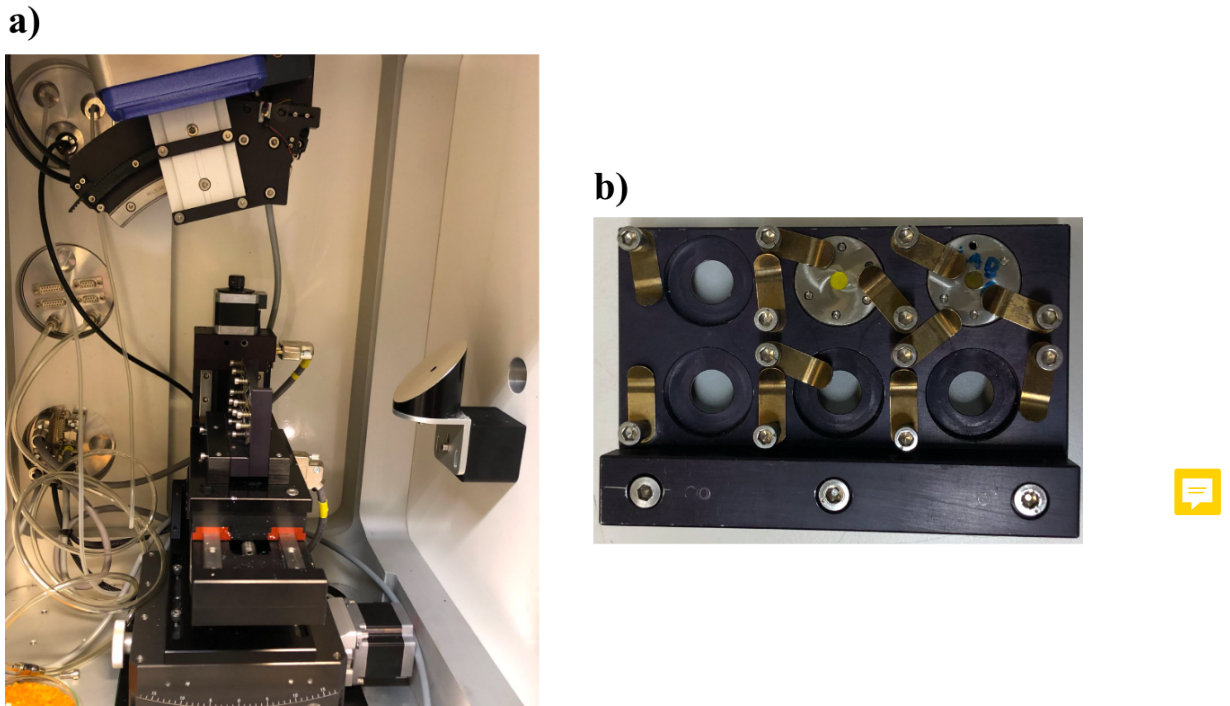


Figure 5.5: a) The inside of the vacuum chamber of the SAXS instrument. The radiation enters from the hole to the right and passes through a sample holder that is mounted to a moving stage in the middle of the figure. Transmitted X-rays are then collected by a detector located to the left of the figure. b) The sandwich cell holder with two sandwich cells mounted in it.

The radially integrated curves were transmission corrected and background subtraction was performed according to

$$I_{\text{subtracted}}(q) = I_{\text{HC}}(q) - I_{\text{background}}(q). \quad (5.1)$$

where $I_{\text{HC}}(q)$ is the intensity of HC electrode samples and $I_{\text{background}}(q)$ is the intensity from samples containing only aluminium. Furthermore, the data from SAXS and WAXS measurements were merged into a single S/WAXS profile, which was possible because of overlap in q -range. The scattering intensity from HC electrodes is believed to be unaffected by the sodiation process in the vicinity of $q = 0.15 \text{ \AA}^{-1}$. Therefore, the S/WAXS profiles were normalized at this q -value.

The intensity in the microporous regime of the (normalized) scattering curve was integrated between $q = 0.19 \text{ \AA}^{-1}$ and $q = 0.5 \text{ \AA}^{-1}$ to minimize the effects of a potential air-exposure affecting the intensity at lower q (see fig. 5.6). More details on the effects of air-exposure can be found in section 6.2.1.

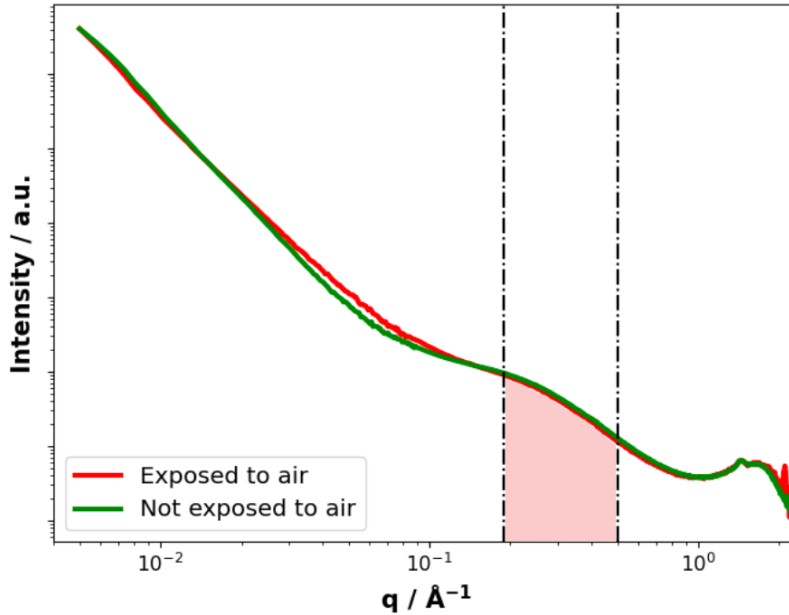


Figure 5.6: Ex situ SWAXS profiles of a sodiated HC where effects from air-exposure can be seen around $q = 0.06 \text{ \AA}^{-1}$. The vertical lines represent the upper and lower bounds of integration.

For analysis of the (002)-peak in the high- q regime the Lorentz-corrected scattering curve $I(q) = I(q)q^2$ was applied [36]. In this q -regime, the scattering curve has a contribution from both a tailing q^{-2} slope from the form factor of lamellar-shaped graphene sheets as well as the structure peak related to the average interlayer spacing between sheets. The Lorentz-corrected scattering curve therefore emphasizes the structure peak from the stacked graphene sheets and is commonly applied to extract the interlayer spacing in lamellar systems such as polymer lamellas in semi-crystalline polymers [37].

5. Methods

6

Results and discussion

In the following chapter the results from the project are presented and discussed. The first section elaborates on the electrochemical characterization of the HC/Na half cells used in this work. In the second section the results from S/WAXS measurements on ex situ HC electrodes are put forth and further analyzed to deduce information about the underlying storage mechanisms that are present during the second sodiation of the HC structure. In the third and final section the results from different cycling conditions are compared to one another and possible changes in the sodiation process are discussed.

6.1 Electrochemical performance of half cells

While results from SAXS measurements can yield invaluable information about the structure of HC, electrochemical techniques provides a different perspective. A better understanding of the redox reactions occurring at the HC electrodes can be gained from the results of cyclic voltammetry and the analysis of the voltage profile can be related to the storage mechanism. Thus a more complete picture can be obtained by combining these methods.

6.1.1 Galvanostatic cycling of coin cells

Figure 6.1 shows the voltage profile of three fully sodiated HC electrodes in cell configurations EC5, EC10 and D10. All three cells show the characteristic electrochemical behavior of an initial slope regime at high voltage followed by a low voltage plateau regime. In each of the three cell configurations, six HC/Na half cells were assembled and cycled to various degrees of sodiation, and the voltage profiles corresponding to the second sodiation of the HC electrode (following the SEI formation cycle) can be seen in figure 6.1b) - d).

In general, the coin cells exhibited adequate reproducibility, with almost identical discharge profiles within each configuration. A noteworthy exception however, is that of the three cells stopped in the plateau region in configuration EC5. Initially all three curves appear to plateau around 0.1 V, but a sudden larger drop in voltage leads to a plateau at just above 0 V. This "plateau drop" occurs at slightly different states of discharge in each cell.

Another visible deviation is that of the cell with cut-off voltage 0.033 V in cell configuration D10. In the sloping region, the curve is slightly offset in voltage, leading to its plateau starting at a lower specific capacity compared the other cells. As a consequence, the capacity fraction stemming from the plateau region in this case becomes very similar to that of the fully discharged cell, despite the higher cut-off voltage of the anomalous cell.

Comparing the voltage profiles of the fully discharged cells, it is clear that the sloping regions are very similar in all configurations, while some differences can be observed in the plateau region. Initially EC5 and EC10 seem to follow the same plateau, but the aforementioned plateau drop leads to a lower plateau for EC5. A lower cut-off voltage nevertheless leads to a higher specific capacity for this configuration compared to EC10. For D10 the plateau is instead higher than that of EC10, leading to a specific capacity of almost 300 mA g^{-1} despite having the same cut-off voltage as EC10.

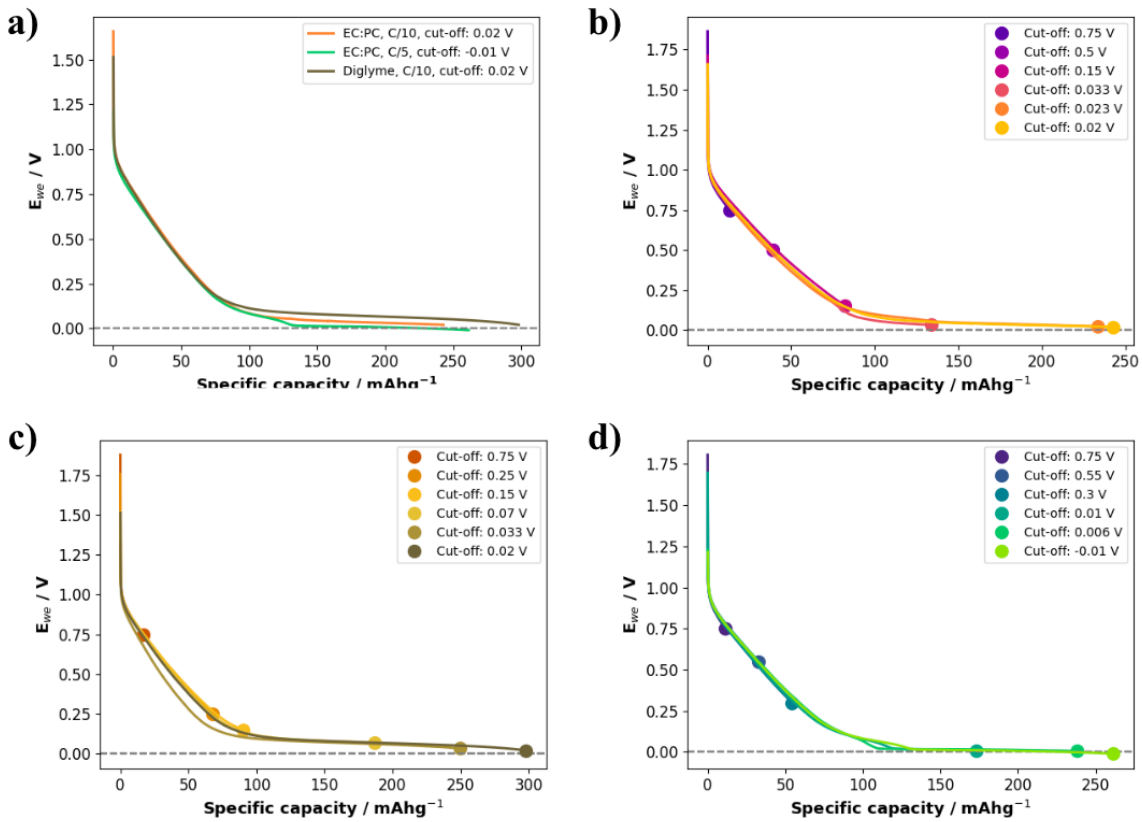


Figure 6.1: Voltage profiles of HC/Na half cells cycled in configuration a) EC5, b) EC10 and c) D10. The dots in a) - c) represent the stopping point of each curve where ex-situ S/WAXS measurements were performed. d) Voltage profile of a fully discharged cell in each of the three configuration.

6.1.2 Slope and plateau capacity contributions

In today's research on SIBs, few authors discuss the voltage profiles of HC electrodes without using the concept of a high voltage slope region and a low voltage plateau region. The definition of these regions is nevertheless rather arbitrary, and the consensus today is that the plateau starts where the voltage drops below 0.1 V (hereon referred to as definition I, see fig. 6.2). As can be seen in figure 6.1d) the voltage profiles can differ even when changing just a single parameter. A poorly defined boundary between the slope and plateau region can thus lead to misrepresentation of results when the definition does not reflect the behavior of each individual voltage profile. It is therefore worthwhile to consider different ways of defining this boundary.

Using definition I, the capacity from the slope and plateau regions in the first three sodiation/desodiations are shown in figure 6.3. In the first sodiation the fractions are very similar between EC10 and D10, with slightly more capacity coming from the plateau than the slope in both configurations. In the first desodiation the slope capacity increases drastically for EC10 while staying relatively unchanged for D10. In the second sodiation the majority of the total capacity comes from the plateau in all three configurations, with EC5 having the greatest contribution from the plateau.



6. Results and discussion

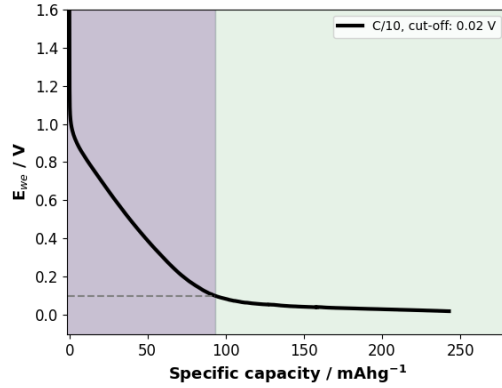


Figure 6.2: Definition I of the slope-plateau boundary, established at $E_{we} = 0.1$ V. The purple background represent the sloping region while the green side represent the plateau region.

When comparing the voltage profiles in figure 6.1d) the plateau capacity contribution appears to be larger for D10, since its plateau reaches further than the others. The reason that EC5 still ends up with more plateau capacity in figure 6.3c) is because of how the boundary between the slope and plateau is defined. Since the plateau appears at a higher voltage in D10, a significant part of the plateau ends up in the sloping region when using definition I, leading to less plateau capacity contribution in this case.

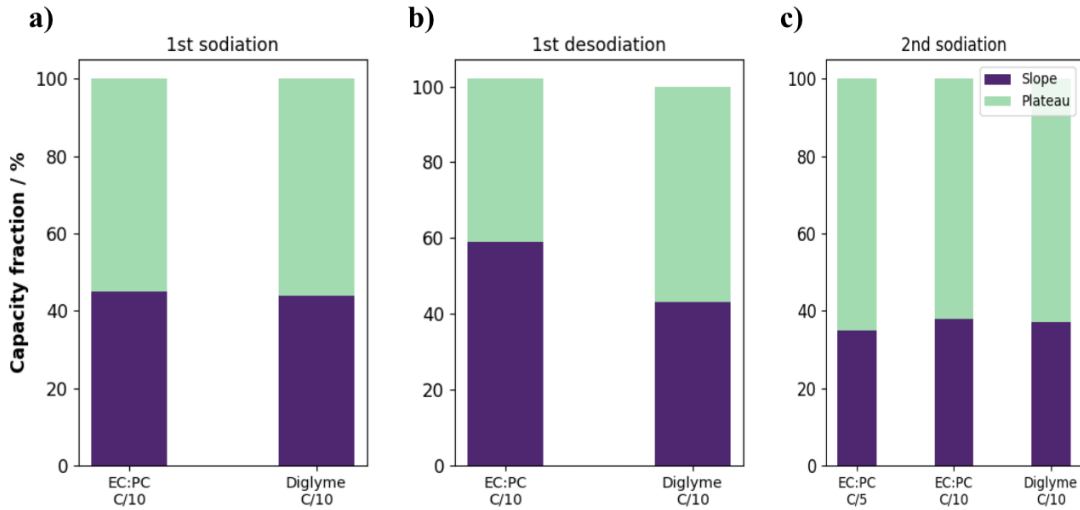


Figure 6.3: The fraction of total capacity stemming from the slope versus plateau region in a) the first sodiation, b) the first desodiation and c) the second sodiation of HC, using definition I of the slope/plateau boundary. In the first sodiation/desodiation EC5 was cycled at C/10 and is therefore identical to EC10.

In an attempt to work around these discrepancies, an alternative way of defining the slope-plateau boundary is proposed in figure 6.4. By drawing two tangent lines that follow the slope and plateau respectively, the boundary can be defined at the x-coordinate at which the two lines intersect. Instead of using a fixed value for all

voltage profiles as in definition I, definition II implies that the boundary is uniquely defined for each individual curve.

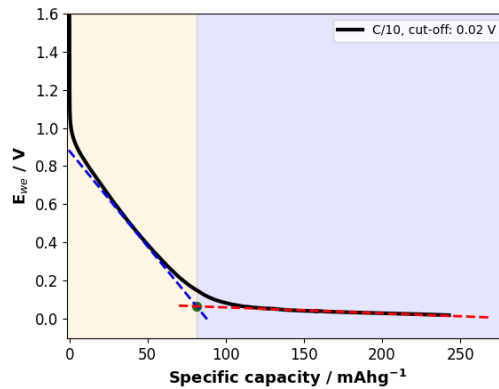


Figure 6.4: Definition II of the slope-plateau boundary, determined by the intersection of two tangent lines that follow the slope (blue tangent) and plateau (red tangent) respectively. The orange background represent the sloping region while the blue side represent the plateau region.

By using definition II, the capacity fractions from the slope and plateau regions in the first three sodiation/desodiations end up as in figure 6.5. In this case the plateau contribution is larger for D10 in all three steps of cycling. For EC10 the slope capacity fraction decreases from the first to the second sodiation, but is still larger than that of EC5 since the plateau of EC10 is cut off earlier. In the first sodiation, SEI formation occurs mainly in the sloping region, leading to the irreversible capacity fade for all configurations. The voltage profiles of the first cycle in every configuration, where SEI formation is visible, can be found in Appendix A.

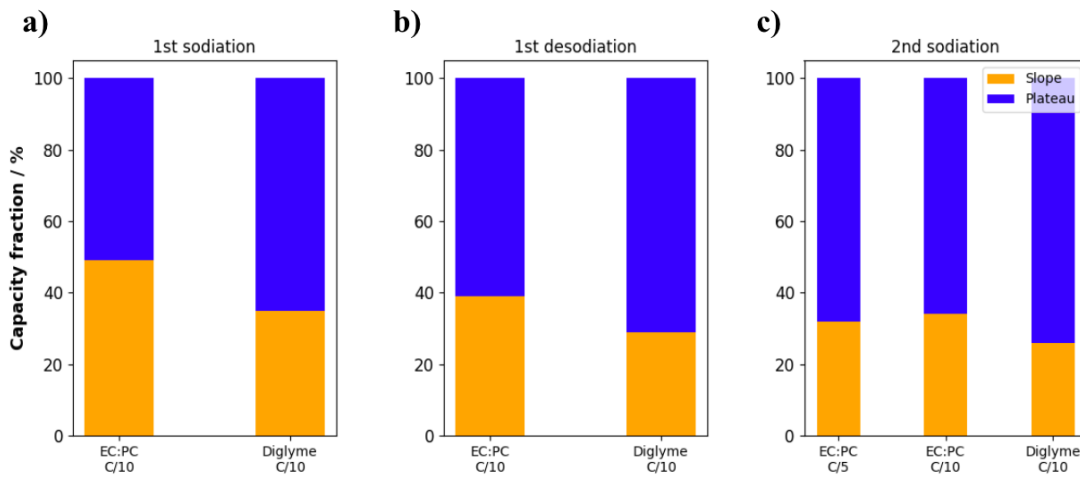


Figure 6.5: The fraction of total capacity stemming from the slope versus plateau region in a) the first sodiation, b) the first desodiation and c) the second sodiation of HC, using definition II of the slope/plateau boundary. In the first sodiation/desodiation EC5 was cycled at C/10 and is therefore identical to EC10.

6.1.3 Cyclic voltammetry and redox reactions

To gain a better understanding of the processes occurring at the HC electrodes, two cyclic voltammograms were generated (one for each of the two electrolytes used in this project) using HC/Na half cells. For both measurements the scanning rate was set to 0.1 mV s^{-1} between 0 V to 2 V, and the resulting voltammograms can be seen in figure 6.6.

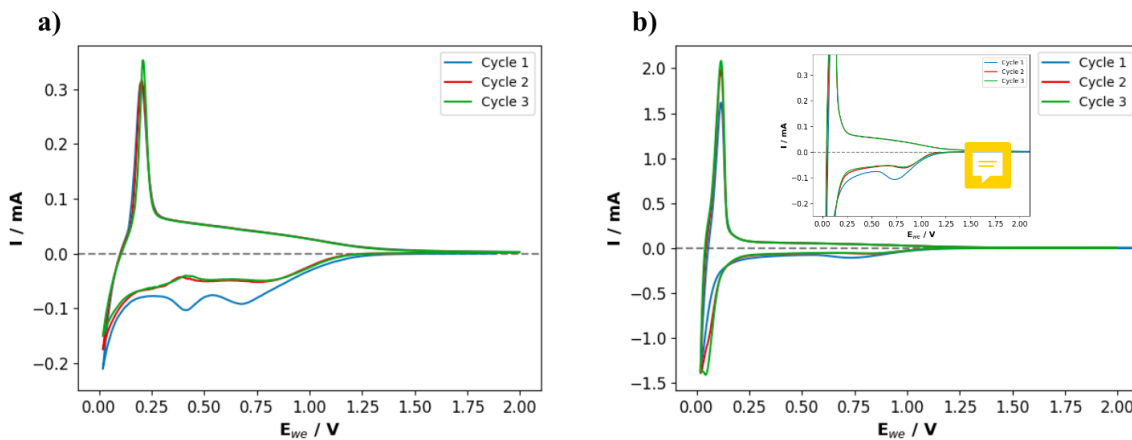


Figure 6.6: Cyclic voltammograms of HC/Na half cells produced with a scanning rate of 0.1 mV s^{-1} . In a) the electrolyte was 1 M NaPF_6 in EC:PC and in b) the electrolyte was 1 M NaPF_6 in diglyme. In the inset of b), the values on the y-axis are the same as in a).

In both voltammograms, broad redox peaks appear in the high voltage region between 1.5 V - 0.3 V, corresponding to the sloping region in galvanostatic cycling. In the low voltage region corresponding to the plateau in the voltage profile, two distinct redox peaks emerge around 0.02 V/0.2 V for the cell with EC:PC as electrolyte solvent, and around 0.02 V/0.1 V in the cell with diglyme. Moreover, the low voltage peaks are almost five times larger in magnitude in the latter. During the first discharge, two additional peaks appear around 0.5 V and 0.75 V in figure 6.6a) and one at about 0.75 V in figure 6.6b). These peaks disappear in subsequent cycles and can be ascribed to the formation of an SEI layer as a consequence of electrolyte decomposition in the cells [38]–[41]. The lack of the peaks in cycle 2 and 3 suggests the stabilization and reproducibility of the sodiation process after the initial formation cycle.

Previous literature ascribe intercalation as the underlying mechanism behind the sharp redox peaks below 0.2 V, and adsorption/desorption of Na-ions at surfaces and edges of graphitic-like domains as the source of the broader peaks in the high voltage region [39]–[41]. Additionally, the gap in voltage between the anodic and cathodic peaks in the low voltage region is smaller for the cell using diglyme as solvent than the one with EC:PC, which suggests faster kinetics in the former [42].

6.2 Hard carbon structural characterization

In this section, results from scattering experiments are presented. First a measurement protocol is developed to ensure reproducibility of ex-situ results. Thereafter, scattering data from measurements on the HC electrodes after galvanostatic cycling to different degree of sodiation (see figure 6.1) are displayed, where changes in the HC electrode structure during the second sodiation can be correlated to different Na storage mechanisms. In the final section, the results from the different cycling configurations are compared to each other to deduce changes in the Na storage mechanisms.

6.2.1 Measurement strategies for reproducibility

In this project, the method of choice to study the sodiation process in HC involves collecting scattering data from a large number of HC electrodes. It is therefore crucial that the effects of outside factors are kept to a minimum to be able to compare the results from measurements on different ex situ samples. Three possible sources of error were therefore investigated: sample-to-sample variations, the effects of washing the electrodes and the consequences of an electrode being exposed to air.

Figure 6.7 shows the S/WAXS profiles of two different pristine HC electrodes, demonstrating sample-to-sample variations. In a), the scattering intensity differ between the two electrodes. This is nevertheless expected since the synthesized electrodes displayed measurable variations in weight, stemming from the coated slurry not being perfectly uniform. A thicker sample yields more scattering and subsequently a higher scattering intensity is expected. To mitigate the differences between sample-to sample variations, the scattering curves are normalized, yielding the results in figure 6.7b). After normalization the two scattering signals are virtually identical, showing that the structure is unchanged between different pristine samples.

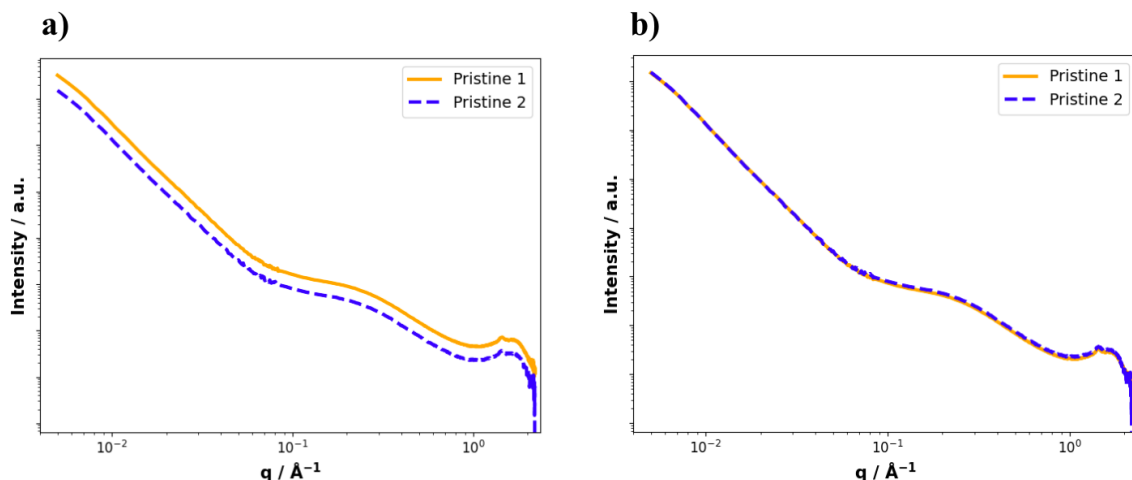


Figure 6.7: Ex situ SWAXS profiles of two pristine HC electrodes a) before normalization and b) after normalization at $q = 0.15 \text{ \AA}^{-1}$.

6. Results and discussion

In figure 6.8, the scattering from a pristine electrode is compared to the HC powder that was used when preparing the electrode slurry. A peak around $q = 1.5 \text{ \AA}^{-1}$ can be observed in the pristine sample but not in the HC powder, which suggests that the scattering that yields this peak stem from some other constituent of the electrode. This peak is attributed to the PVDF binder in the electrode [43].

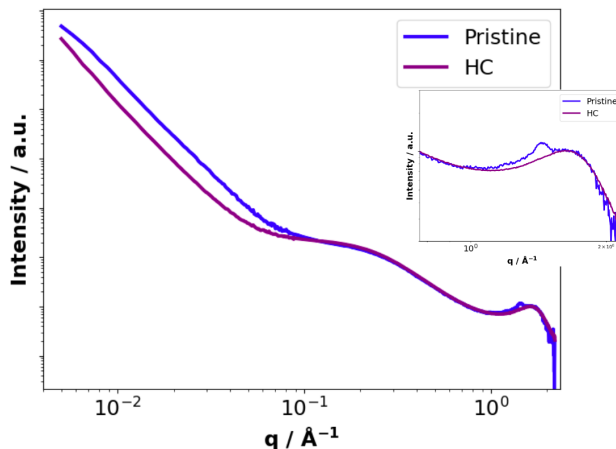


Figure 6.8: Ex situ WAXS profiles of a pristine electrode and the HC powder used to synthesize the HC electrode slurry. The peak around $q = 1.5 \text{ \AA}^{-1}$ is attributed to the polymer binder used in the slurry mix.

Figure 6.9 shows the scattering from a washed and unwashed electrode after being assembled in a coin cell. To minimize effects of sample-to-sample variations, measurements were done on the same electrode by cutting a semi-sodiated HC electrode in half and wash only one of the halves. In the unwashed electrode the residues of dried salt and SEI compounds give strong contributions to the scattering curve as shown by e.g. the increased intensity at high q , corresponding to more material in the electrode. The washing of the HC structure is therefore necessary to extract the scattering contribution from the sodiated HC electrode.

Figure 6.10 shows the results from measurements on a fully sodiated HC electrode exposed to air. The electrode was washed and then cut in half, and one of the halves were left in air for 1 h. From the exposed sample, a slight increase in scattering intensity can be observed at the end of the particle regime in the vicinity of $q = 0.07 \text{ \AA}^{-1}$, and a sharp peak emerges around $q = 2.1 \text{ \AA}^{-1}$. This peak is believed to be the result of NaOH forming in the electrode when Na reacts with H₂O from the air. Similar peaks have been observed in previous studies on sodiated HC electrodes exposed to air [13]. Hindering exposure from air is therefore crucial to make an accurate analysis of the structural changes following sodiation and the lack of the identified signatures at $q = 0.07 \text{ \AA}^{-1}$ can be used to validate the measurement of an intact electrode.

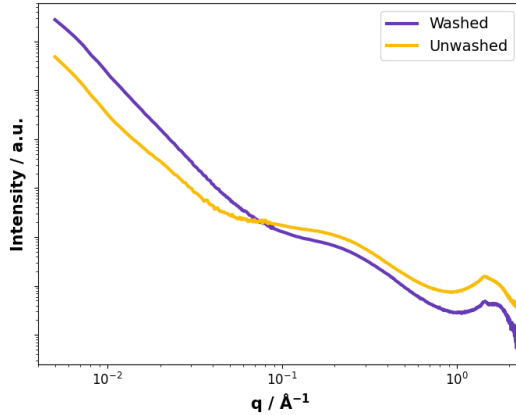


Figure 6.9: Ex situ SWAXS profiles of a cycled HC electrode where one half of the electrode was washed and the other was not.

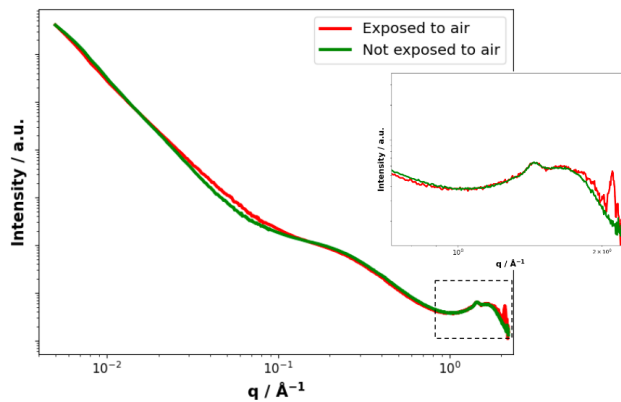


Figure 6.10: Ex situ SWAXS profiles of a sodiated HC electrode where one half of the electrode was exposed to air for 1 h. The inset shows an enlarged view of the high- q region where a peak emerging around $q = 2.1 \text{ \AA}^{-1}$ can be observed in the exposed sample.

6.2.2 Scattering from HC electrodes

Figure 6.11 shows the S/WAXS curves of ex situ electrodes sodiated to different degrees of sodiation for the three conditions EC5, EC10 and D10 (the corresponding voltage profiles are shown in figure 6.1). The curves are normalized at $q = 0.15 \text{ \AA}^{-1}$ to compensate for sample-to-sample variations. The overall shape of the characteristic hard carbon structure is seen in all profiles entailing a slope region from the surface of the HC particles at low q , the shoulder from the microporosity at intermediate q , and the (002)-peak from stacked graphene sheets at high q . A potential exposure to trace amounts of H_2O lead to an increase in signal intensity around $q = 0.07 \text{ \AA}^{-1}$ for all samples in configuration D10, and the 91% sodiated sample in EC5.

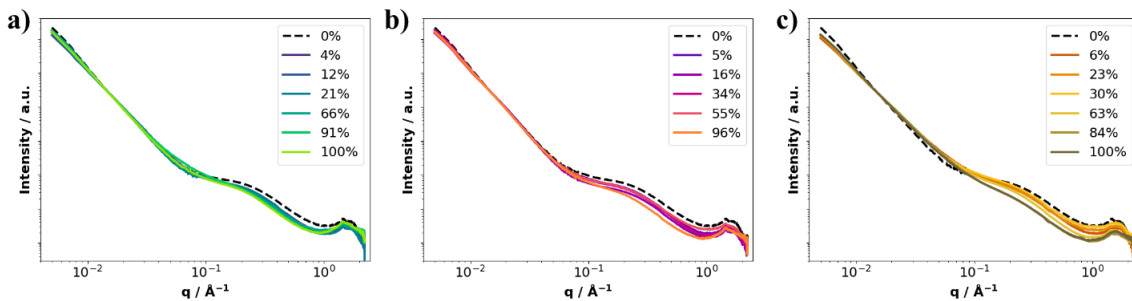


Figure 6.11: S/WAXS profiles from ex situ measurements on HC electrodes used in galvanostatic cycling of coin cells in configuration a) EC5, b) EC10 and c) D10.

To study the structural changes in more detail, scattering in the different regimes can be analyzed separately. Storage of Na-ions in the porous structure of HC can be understood by analyzing the intermediate- q region of scattering curves. A loss of signal intensity in this region means less contrast between the pores and their surrounding carbon matrix (as seen by the factor $(\rho_p - \rho_m)^2$ in eq. 4.3), suggesting the presence of Na-ions in the pores.

As a first qualitative analysis of the microporous regime, the scattering signal from a pristine HC electrode (placed in a battery and washed, but not cycled) was subtracted from the SWAXS profiles of HC electrodes used in galvanostatic cycling of coin cells (see fig. 6.1). If the pores in HC were to remain unaltered by the sodiation process, the scattering signal of the sodiated electrodes would equal that of the pristine sample in this q -range, and the subtracted signal would simply be a flat line at intensity 0. Conversely, any decrease in contrast due to pore filling would lead to a negative intensity for the subtracted signal. Furthermore, the q -value at which scattering intensity loss is observed can be correlated to the average size of the pores. A drop in intensity at lower q -values indicate Na filling in larger pores than if the intensity drops at higher q .

The subtracted scattering signals can be seen in figure 6.12. A non-uniform loss of intensity can be observed in all three configurations, implying that Na-ions do

not fill larger and smaller pores uniformly. As the degree of sodiation increases, a shift in the curve minima can be observed in configurations EC5 and D10, while no obvious shift can be observed in EC10. For EC5, the minima tends to higher q-values, suggesting that smaller pores become more favorable for Na-ion storage in the later stages of HC sodiation at higher charge rates. On the contrary, the minima can be seen shifting to lower q-values in configuration D10, which would indicate that larger pores get more utilized for Na storage at higher degrees of sodiation when using diglyme as electrolyte solvent. This trend with the curve shifting to lower q-values have been observed previously at a charge rate of C/20 where the electrolyte was 1 M NaPF₆ in EC:DMC [14].

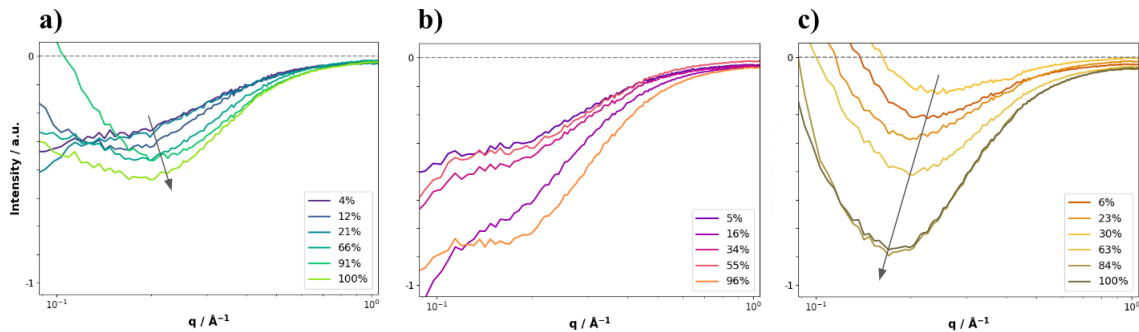


Figure 6.12: Scattering profiles in the microporous regime from ex situ measurements on HC electrodes used in galvanostatic cycling of coin cells in configuration a) EC5, b) EC10 and c) D10. All curves have been subtracted by the signal from a pristine HC electrode. Note that a potential exposure to trace amounts of H₂O lead to an increase in signal intensity around $q = 0.07 \text{\AA}^{-1}$ for all samples in configuration D10, and the 91 % sodiated sample in EC5.

In figure 6.13, the microporous regimes are plotted without subtraction of the pristine sample. Below each figure is a corresponding plot of the integrated intensity of each curve as a function of degree of sodiation, normalized such that the integrated intensity of the pristine sample is unity. As mentioned in section 5.3, the integration limits were chosen as $0.19 \text{\AA}^{-1} < q < 0.5 \text{\AA}^{-1}$ to avoid other factors such as air exposure affecting the results. Other integration limits were tested, but no distinct changes in broader tendencies of the results could be observed.

For all three configurations, the overall trends are similar in figures d) - f). The integrated intensity of the microporous region decreases immediately at low degrees of sodiation, followed by an increase in the vicinity of the voltage profile transitioning from slope to plateau. After that the intensity continues to decrease until the electrode is fully sodiated. Compared to the other configurations, EC5 displays less decrease of the integrated intensity in both the plateau and sloping region, suggesting less pore filling is present at higher charge rates.

One possible way of explaining the sudden increase of integrated intensity when the voltage profile transitions from slope to plateau is by thinking in terms of the

6. Results and discussion

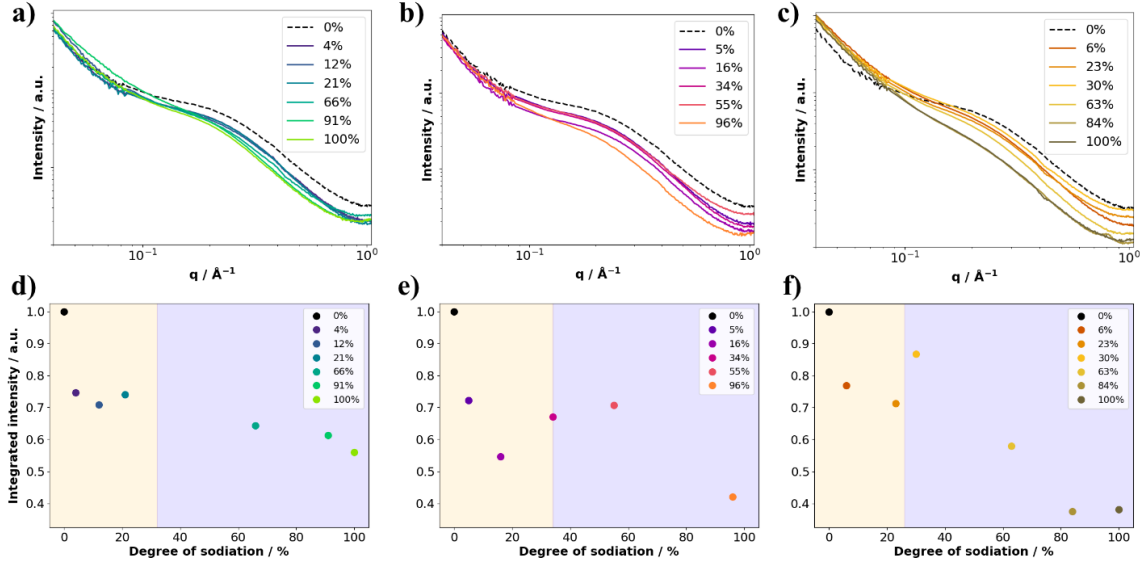


Figure 6.13: Scattering profiles in the microporous regime from ex situ measurements on HC electrodes used in galvanostatic cycling of coin cells in configuration a) EC5, b) EC10 and c) D10. The integrated intensity of each curve (between $0.19 \text{\AA}^{-1} < q < 0.5 \text{\AA}^{-1}$) as a function of degree of sodiation are shown in the corresponding figure below a) - c). The colors in the background of figure d) - f) indicate where the voltage profile transitions from the sloping region (orange) to the plateau region (blue).

underlying storage mechanisms. If pore filling is the dominant mechanism in the sloping region, a decreasing scattering intensity is expected as a consequence of the decreasing contrast between pores and surrounding matrix. As can be deduced from the cyclic voltammograms (fig. 6.6) however, an additional storage mechanism starts to take place below a certain threshold voltage. Hypothesizing that this mechanism is intercalation, and that it starts to compete with the pore filling mechanism when the voltage profile transitions from slope to plateau, the scattering intensity could then increase when the electron density of the carbon matrix increases as a result of the inserted Na-ions. This is because the denser matrix could yield a larger scattering contrast between pores and matrix, and if intercalation suddenly becomes more prominent than the pore filling mechanism, the contrast could increase on average even if both mechanisms are occurring at the same time.

In the atomic structure regime of the SWAXS profile, distances down to the atomic scale can be probed. As discussed in section 4.2, the (002)-peak that appears around $q = 1.7 \text{\AA}^{-1}$ is related to the average distance between graphene sheets in the HC structure, and the peak width and position yields information about the distribution of those interplanar distances. If the average distance between sheets were to increase, the (002)-peak would shift towards lower q -values, and vice versa.

Lorentz-corrected WAXS profiles from measurements on HC electrodes can be seen in figure 6.14. In all figures, the signal from the pristine electrode is plotted for

reference. In the pristine profile, the (002)-peak is clearly visible at $q = 1.73 \text{ \AA}^{-1}$.

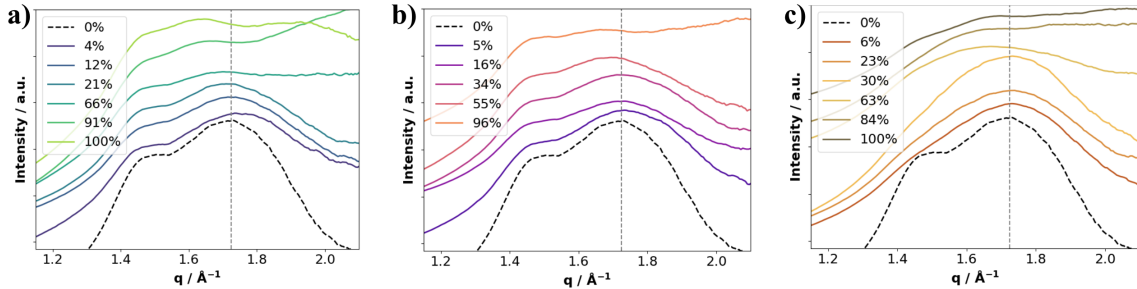


Figure 6.14: Lorentz-corrected WAXS profiles from ex situ measurements on HC electrodes used in galvanostatic cycling of coin cells in configuration a) EC5, b) EC10 and c) D10. The dashed vertical lines indicate the peak position of the pristine HC electrode.

At low degrees of sodiation, little to no shift in the (002)-peak can be observed in any of the three cycling configurations. For higher degrees of sodiation however, the peak tends towards lower q -values. This would suggest that the average interplanar distances remains unaltered in the sloping region of the voltage profile, but increases somewhat in the plateau region. Moreover, the shift is most obvious in configurations EC5 and D10, implying that the interlayer distance increases more at higher charge rates and when using diglyme as electrolyte solvent.

The presence of a broad peak at $q = 2 \text{ \AA}^{-1}$ can be attributed to densely packed Na in the porous structure which form quasi-metallic clusters with a packing density orderly enough for a broad scattering peak to emerge at high q -values [13]. This suggests extensive pore filling at higher degree of sodiation in all configurations.

6.3 Inferred storage mechanisms from electrochemistry and scattering

The two storage mechanisms that primarily can be inferred from the gathered data are the pore filling mechanism and the insertion mechanism. It is nevertheless important to emphasize that with the tools at hand, other storage mechanisms such as adsorption at defects and edges are harder to detect, and that prior beliefs can affect the interpretation of such results. That said, the distinction between the different storage mechanisms sometimes become rather diffuse (especially when interpreting SWAXS data), and a separate discussion could be held regarding for example the differences between what is to be considered a Na-ion adsorbing to a defect in a graphene sheet (possibly facing a pore in the structure) and a Na-ion being stored inside a pore. It is also possible that a Na-ion adsorbing at a defect could affect the interplanar distances of surrounding graphene layers. Putting all of this into consideration, the rest of this section will be dedicated to comparing the results

6. Results and discussion

from the electrochemical experiments with the scattering data, as well as discussing if and how the Na storage appears to change in the different cycling configurations.

In all three configuration, the general trends suggest that the pore filling mechanism is present along the whole voltage profile, and that intercalation of Na-ions becomes more prominent in the plateau region. This interpretation is based on the assumption that insertion of Na-ions into graphite-like domains is the underlying storage mechanism leading to increasing interlayer distances, and that pore filling is the mechanism leading to less scattering in the microporous domain of the SWAXS profile. When reaching higher degrees of sodiation, clustering of Na-ions in the micropores also becomes clearly visible in the WAXS signal. Moreover these trends match well with the results from the CV experiments, in which the broad and sharp redox peaks would correspond to pore filling in a broad voltage range (encompassing both slope and plateau), and intercalation appearing at low voltages (i.e. the plateau region).

This work is not the first to utilize S/WAXS for studying the sodiation process in HC. Morikawa et al. [13] used the technique to study HCs prepared at various heat treatment temperatures. By performing S/WAXS measurements at different degrees of sodiation they could correlate changes in the signal with changes in the structure due to the storage of Na-ions. They found that sodiation occurred in the graphite-like domains, on graphene defects and in micropores, but the degree to which the different storage mechanisms contributed to the overall storage capacity varied depending on the heat treatment temperature. Similarly, Kitsu Iglesias et al. [14] used in operando SAXS to study the Na storage in the pores of HC during battery operation. They concluded that a higher volume fraction of closed pores in the structure leads to a higher plateau capacity, and that intercalation occurs simultaneously with the pore filling mechanism in the plateau region. Furthermore, it was found that the pores fill non-uniformly, with some pores possibly being inaccessible for the Na-ions.

6.4 Differences in the sodiation process

Regarding differences in the Na storage mechanisms at a higher charge rate, the results points in the direction that less pore filling takes place at C/5 than in C/10. In particular, the larger pores are less utilized at higher rates, and instead, slightly more Na insertion is occurring. One possible explanation for this behavior is that the faster kinetics and larger bombardment of Na-ions leads to them having less time and space to be transported further into the structure. Instead they cluster together and clog narrow spaces such as graphite-like domains and smaller pores, obstructing the pathways for subsequent Na-ions and making it harder to reach some of the larger pores that may be located deeper inside the HC structure.

When diglyme is used as electrolyte solvent instead of EC:PC, the specific capacity of the coin cells increases by roughly 20 % in the second sodiation. Compared to EC10, the plateau contribution of D10 is the main reason for this increase. When

comparing the results from the scattering experiments, there seems to be little to no difference in contribution from pore filling, while there could be slightly more Na insertion for D10. This would also explain why the scattering intensity from the porous region increases more drastically in D10 when the voltage profile transitions from slope to plateau (see fig. 6.13), assuming that the increase is a result of the insertion mechanism kicking in. Moreover, these findings fit well together with the hypothesis that diglyme-based electrolytes can help facilitate cointercalation of Na-ions in graphite-like structures [26]–[29].

6. Results and discussion

7

Conclusions and outlook

In this thesis project, the sodiation process in HC was studied by using S/WAXS together with electrochemical techniques. The results suggests that a "filling-intercalation model" could describe the sodiation process in the studied HC electrodes. More specifically the pore filling mechanism appears to be present during the whole sodiation process, while the two mechanisms compete along the plateau region of the voltage profile. Comparing the different charge rates and electrolytes, no obvious alterations in the pore filling mechanism could be observed along the sloping region. Cells using diglyme as electrolyte solvent retained a higher specific capacity than those using EC:PC, possibly due to the enabling of more intercalation along the plateau region. More generally, the results suggest that the sodiation process in HC electrodes could depend on not only the structure of the material, but a variety of parameters in the system as a whole.

As previously discussed, the body of research on the sodiation process in HC is more times than not contradictory. The results from this thesis oppose prior studies and suggests an alternative sodiation mechanism in the current systems than previously proposed. This highlights even more so the need to classify and subdivide HCs derived from different precursors, in order to make it more transparent to material scientists what precise microstructure they are dealing with. By achieving a clearer understanding of the structure-storage correlation, a more sophisticated engineering of HC electrodes can lead to better performing SIBs in the future. In this way, the batteries could pose as a cheap and environmentally friendly complement to the LIB technology in the energy storage landscape.

7. Conclusions and outlook

References

- [1] M. Winter, B. Barnett, and K. Xu, “Before Li ion batteries,” *Chemical Reviews*, vol. 118, no. 23, pp. 11433–11456, 2018. DOI: [10.1021/acs.chemrev.8b00422](https://doi.org/10.1021/acs.chemrev.8b00422).
- [2] X. Dou, I. Hasa, D. Saurel, *et al.*, “Hard carbons for sodium-ion batteries: Structure, analysis, sustainability, and electrochemistry,” *Materials Today*, vol. 23, pp. 87–104, 2019, ISSN: 1369-7021. DOI: <https://doi.org/10.1016/j.mattod.2018.12.040>.
- [3] G. H. Newman and L. P. Kleemann, “Ambient temperature cycling of an Na-TiS₂ cell,” *Journal of The Electrochemical Society*, vol. 127, no. 10, p. 2097, Oct. 1980. DOI: [10.1149/1.2129353](https://doi.org/10.1149/1.2129353).
- [4] N. Yabuuchi, K. Kubota, M. Dahbi, and S. Komaba, “Research development on sodium-ion batteries,” *Chemical Reviews*, vol. 114, no. 23, pp. 11636–11682, 2014, PMID: 25390643. DOI: [10.1021/cr500192f](https://doi.org/10.1021/cr500192f).
- [5] E. Goikolea, V. Palomares, S. Wang, *et al.*, “Na-ion batteries—approaching old and new challenges,” *Advanced Energy Materials*, vol. 10, no. 44, p. 2002055, 2020. DOI: <https://doi.org/10.1002/aenm.202002055>.
- [6] A. Gomez-Martin, J. Martinez-Fernandez, M. Ruttert, M. Winter, T. Placke, and J. Ramirez-Rico, “Correlation of structure and performance of hard carbons as anodes for sodium ion batteries,” *Chemistry of Materials*, vol. 31, no. 18, pp. 7288–7299, 2019. DOI: [10.1021/acs.chemmater.9b01768](https://doi.org/10.1021/acs.chemmater.9b01768).
- [7] H. Moon, A. Innocenti, H. Liu, *et al.*, “Bio-waste-derived hard carbon anodes through a sustainable and cost-effective synthesis process for sodium-ion batteries,” *ChemSusChem*, vol. 16, no. 1, e202201713, 2023. DOI: <https://doi.org/10.1002/cssc.202201713>.
- [8] X. Dou, C. Geng, D. Buchholz, and S. Passerini, “Research Update: Hard carbon with closed pores from pectin-free apple pomace waste for Na-ion batteries,” *APL Materials*, vol. 6, no. 4, p. 047501, Jan. 2018, ISSN: 2166-532X. DOI: [10.1063/1.5013132](https://doi.org/10.1063/1.5013132).
- [9] F. S. Genier, S. Pathreker, R. L. Schuarca, M. Islam, and I. D. Hosein, “Hard carbon derived from avocado peels as a high-capacity, fast na⁺ diffusion anode material for sodium-ion batteries,” *ECS Advances*, vol. 1, no. 3, p. 030502, Aug. 2022. DOI: [10.1149/2754-2734/ac8aaf](https://doi.org/10.1149/2754-2734/ac8aaf).
- [10] Mohit and S. Hashmi, “Hard carbon anode derived from pre-treated bio-waste sugarcane bagasse for high capacity sodium-ion battery fabricated with bio-degradable porous polymer electrolyte,” *Journal of Energy Storage*, vol. 83, p. 110694, 2024, ISSN: 2352-152X. DOI: <https://doi.org/10.1016/j.est.2024.110694>.

- [11] P. Willmott, *An Introduction to Synchrotron Radiation : Techniques and Applications*. John Wiley Sons, Incorporated, 2019, ISBN: 9781119280378.
- [12] H. Schnablegger and Y. Singh, *The SAXS Guide*, 5th ed. Anton Paar GmbH, 2023.
- [13] Y. Morikawa, S.-i. Nishimura, R.-i. Hashimoto, M. Ohnuma, and A. Yamada, "Mechanism of sodium storage in hard carbon: An x-ray scattering analysis," *Advanced Energy Materials*, vol. 10, no. 3, p. 1903176, 2020. DOI: <https://doi.org/10.1002/aenm.201903176>.
- [14] L. Kitsu Iglesias, E. N. Antonio, T. D. Martinez, *et al.*, "Revealing the sodium storage mechanisms in hard carbon pores," *Advanced Energy Materials*, vol. 13, no. 44, p. 2302171, 2023. DOI: <https://doi.org/10.1002/aenm.202302171>.
- [15] B. Scrosati, "Lithium batteries: From early stages to the future," in *Lithium Batteries*. John Wiley Sons, Ltd, 2013, ch. 2, pp. 21–38, ISBN: 9781118615515. DOI: <https://doi.org/10.1002/9781118615515.ch2>.
- [16] E. C. Cengiz, J. Rizell, M. Sadd, A. Matic, and N. Mozhzhukhina, "Review—reference electrodes in li-ion and next generation batteries: Correct potential assessment, applications and practices," *Journal of The Electrochemical Society*, vol. 168, no. 12, p. 120539, Dec. 2021. DOI: [10.1149/1945-7111/ac429b](https://doi.org/10.1149/1945-7111/ac429b).
- [17] R. Usiskin, Y. Lu, J. Popovic, *et al.*, "Fundamentals, status and promise of sodium-based batteries," *Nature Reviews Materials*, vol. 6, no. 11, pp. 1020–1035, Nov. 2021. DOI: [10.1038/s41578-021-00324-w](https://doi.org/10.1038/s41578-021-00324-w).
- [18] H. Zhang, Y. Yang, D. Ren, L. Wang, and X. He, "Graphite as anode materials: Fundamental mechanism, recent progress and advances," *Energy Storage Materials*, vol. 36, pp. 147–170, 2021, ISSN: 2405-8297. DOI: <https://doi.org/10.1016/j.ensm.2020.12.027>.
- [19] Y. Li, Y. Lu, P. Adelhelm, M.-M. Titirici, and Y.-S. Hu, "Intercalation chemistry of graphite: Alkali metal ions and beyond," *Chem. Soc. Rev.*, vol. 48, pp. 4655–4687, 17 2019. DOI: [10.1039/C9CS00162J](https://doi.org/10.1039/C9CS00162J).
- [20] K. Nobuhara, H. Nakayama, M. Nose, S. Nakanishi, and H. Iba, "First-principles study of alkali metal-graphite intercalation compounds," *Journal of Power Sources*, vol. 243, pp. 585–587, 2013, ISSN: 0378-7753. DOI: <https://doi.org/10.1016/j.jpowsour.2013.06.057>.
- [21] Y. Liu, B. V. Merinov, and W. A. Goddard, "Origin of low sodium capacity in graphite and generally weak substrate binding of Na and Mg among alkali and alkaline earth metals," *Proceedings of the National Academy of Sciences of the United States of America*, vol. 113, no. 14, pp. 3735–3739, 2016. DOI: [10.1073/pnas.1602473113](https://doi.org/10.1073/pnas.1602473113).
- [22] O. Lenchuk, P. Adelhelm, and D. Mollenhauer, "New insights into the origin of unstable sodium graphite intercalation compounds," *Phys. Chem. Chem. Phys.*, vol. 21, pp. 19378–19390, 35 2019. DOI: [10.1039/C9CP03453F](https://doi.org/10.1039/C9CP03453F).
- [23] M. Dahbi, N. Yabuuchi, K. Kubota, K. Tokiwa, and S. Komaba, "Negative electrodes for Na-ion batteries," *Phys. Chem. Chem. Phys.*, vol. 16, pp. 15007–15028, 29 2014. DOI: [10.1039/C4CP00826J](https://doi.org/10.1039/C4CP00826J).

- [24] Z. Lin, Q. Xia, W. Wang, W. Li, and S. Chou, “Recent research progresses in ether- and ester-based electrolytes for sodium-ion batteries,” *InfoMat*, vol. 1, no. 3, pp. 376–389, 2019. DOI: <https://doi.org/10.1002/inf2.12023>.
- [25] A. Ponrouch, E. Marchante, M. Courty, J.-M. Tarascon, and M. R. Palacín, “In search of an optimized electrolyte for na-ion batteries,” *Energy Environ. Sci.*, vol. 5, pp. 8572–8583, 9 2012. DOI: 10.1039/C2EE22258B.
- [26] B. Jache and P. Adelhelm, “Use of graphite as a highly reversible electrode with superior cycle life for sodium-ion batteries by making use of co-intercalation phenomena,” *Angewandte Chemie International Edition*, vol. 53, no. 38, pp. 10 169–10 173, 2014. DOI: <https://doi.org/10.1002/anie.201403734>.
- [27] J. Zhang, D.-W. Wang, W. Lv, *et al.*, “Achieving superb sodium storage performance on carbon anodes through an ether-derived solid electrolyte interphase,” *Energy Environ. Sci.*, vol. 10, pp. 370–376, 1 2017. DOI: 10.1039/C6EE03367A.
- [28] A. P. Cohn, K. Share, R. Carter, L. Oakes, and C. L. Pint, “Ultrafast solvent-assisted sodium ion intercalation into highly crystalline few-layered graphene,” *Nano Letters*, vol. 16, no. 1, pp. 543–548, 2016. DOI: 10.1021/acs.nanolett.5b04187.
- [29] H. Kim, J. Hong, Y.-U. Park, J. Kim, I. Hwang, and K. Kang, “Sodium storage behavior in natural graphite using ether-based electrolyte systems,” *Advanced Functional Materials*, vol. 25, no. 4, pp. 534–541, 2015. DOI: <https://doi.org/10.1002/adfm.201402984>.
- [30] X. Chen, C. Liu, Y. Fang, *et al.*, “Understanding of the sodium storage mechanism in hard carbon anodes,” *Carbon Energy*, vol. 4, pp. 1133–1150, 6 2022. DOI: 10.1002/cey2.196.
- [31] J. Kipling, J. Sherwood, P. Shooter, and N. Thompson, “The pore structure and surface area of high-temperature polymer carbons,” *Carbon*, vol. 1, no. 3, pp. 321–328, 1964, ISSN: 0008-6223. DOI: [https://doi.org/10.1016/0008-6223\(64\)90286-6](https://doi.org/10.1016/0008-6223(64)90286-6).
- [32] D. A. Stevens and J. R. Dahn, “High capacity anode materials for rechargeable sodium-ion batteries,” *Journal of The Electrochemical Society*, vol. 147, no. 4, p. 1271, Apr. 2000. DOI: 10.1149/1.1393348.
- [33] D. A. Stevens and J. R. Dahn, “The mechanisms of lithium and sodium insertion in carbon materials,” *Journal of The Electrochemical Society*, vol. 148, no. 8, A803, Jun. 2001. DOI: 10.1149/1.1379565.
- [34] B. Zhang, C. M. Ghimbeu, C. Laberty, C. Vix-Guterl, and J.-M. Tarascon, “Correlation between microstructure and Na storage behavior in hard carbon,” *Advanced Energy Materials*, vol. 6, no. 1, p. 1501588, 2016. DOI: <https://doi.org/10.1002/aenm.201501588>.
- [35] L. Gehrlein, “Enhancing the performance of si/gr anodes by evaluating the impact of electrolyte formulations on the solid electrolyte interphase,” 38.02.01; LK 01, Ph.D. dissertation, Karlsruher Institut für Technologie (KIT), 2022, 170 pp. DOI: 10.5445/IR/1000151010.
- [36] M. Camara, K. Rishi, G. Beauchage, and S. K. Sukumaran, “A scattering function for correlated lamellae,” *Polymer*, vol. 237, p. 124 281, 2021, ISSN: 0032-3861. DOI: <https://doi.org/10.1016/j.polymer.2021.124281>.

- [37] F. Cser, “About the lorentz correction used in the interpretation of small angle x-ray scattering data of semicrystalline polymers,” *Journal of Applied Polymer Science*, vol. 80, no. 12, pp. 2300–2308, 2001. DOI: <https://doi.org/10.1002/app.1335>.
- [38] T. Zhang, J. Mao, X. Liu, *et al.*, “Pinecone biomass-derived hard carbon anodes for high-performance sodium-ion batteries,” *RSC Advances*, vol. 7, pp. 41 504–41 511, 2017. [Online]. Available: <https://api.semanticscholar.org/CorpusID:54502153>.
- [39] L. Pei, H. Cao, L. Yang, *et al.*, “Hard carbon derived from waste tea biomass as high-performance anode material for sodium-ion batteries,” *Ionics*, vol. 26, no. 1, pp. 5535–5542, 2020. DOI: <https://doi.org/10.1007/s11581-020-03723-1>.
- [40] H. Yang, R. Xu, and Y. Yu, “A facile strategy toward sodium-ion batteries with ultra-long cycle life and high initial coulombic efficiency: Free-standing porous carbon nanofiber film derived from bacterial cellulose,” *Energy Storage Materials*, vol. 22, pp. 105–112, 2019, ISSN: 2405-8297. DOI: <https://doi.org/10.1016/j.ensm.2019.01.003>.
- [41] Y. Zhang, X. Li, P. Dong, *et al.*, “Honeycomb-like hard carbon derived from pine pollen as high-performance anode material for sodium-ion batteries,” *ACS Applied Materials & Interfaces*, vol. 10, no. 49, pp. 42 796–42 803, 2018. DOI: [10.1021/acsami.8b13160](https://doi.org/10.1021/acsami.8b13160).
- [42] F. Wang, T. Zhang, and F. Ran, “Insights into sodium-ion batteries through plateau and slope regions in cyclic voltammetry by tailoring bacterial cellulose precursors,” *Electrochimica Acta*, vol. 441, p. 141 770, 2023, ISSN: 0013-4686. DOI: <https://doi.org/10.1016/j.electacta.2022.141770>.
- [43] Q. Zhang, Z. Sha, X. Cui, *et al.*, “Incorporation of redox-active polyimide binder into lifepo₄ cathode for high-rate electrochemical energy storage,” *Nanotechnology Reviews*, vol. 9, no. 1, pp. 1350–1358, 2020. DOI: [doi:10.1515/ntrev-2020-0092](https://doi.org/10.1515/ntrev-2020-0092).

A

Formation cycle of coin cells

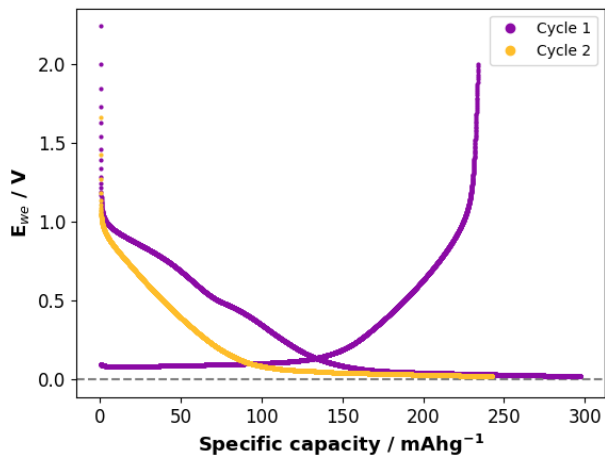


Figure A.1: Formation cycle and the second discharge of a HC/Na half cell cycled in configuration EC10. A large capacity fade is observed, likely due to SEI formation during the first discharge.

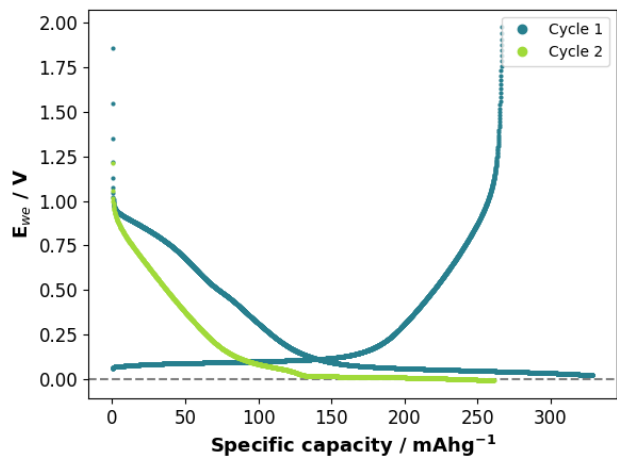


Figure A.2: Formation cycle and the second discharge of a HC/Na half cell cycled in configuration EC5. A large capacity fade is observed, likely due to SEI formation during the first discharge.

A. Formation cycle of coin cells

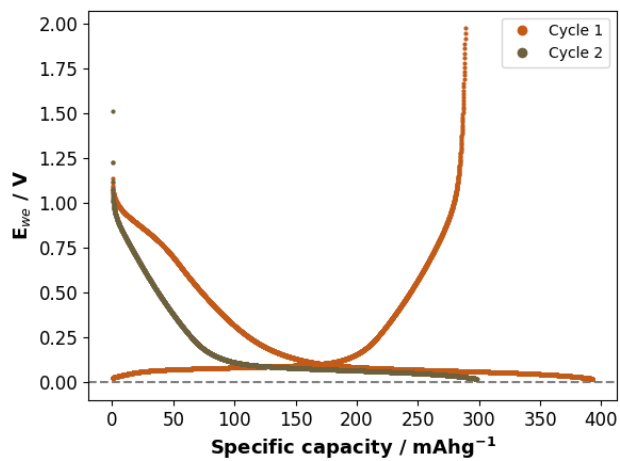


Figure A.3: Formation cycle and the second discharge of a HC/Na half cell cycled in configuration D10. A large capacity fade is observed, likely due to SEI formation during the first discharge.

B

Voltage profiles of symmetric cells

Previous studies have shown that high overpotentials can arise when Na metal is used as CE in SIBs [16]. This can lead to polarization of the measured voltage when a two-electrode cell is used, since the CE also serves as the RE in such a configuration.

In this project, finding a suitable cut-off voltage is crucial for ensuring that the desired degree of sodiation is reached in the HC electrodes. High overpotentials could lead to unpredictable behavior of the HC/Na half cells, especially in the plateau region where small changes in potential can lead to vastly different outcomes of measurements. To investigate the possibility of such overpotentials, symmetric Na/Na cells (with 1 M NaPF₆ in EC:PC (1:1 by wt.) as electrolyte) were cycled at various charge densities. The results of these measurements can be seen in figure B.1.

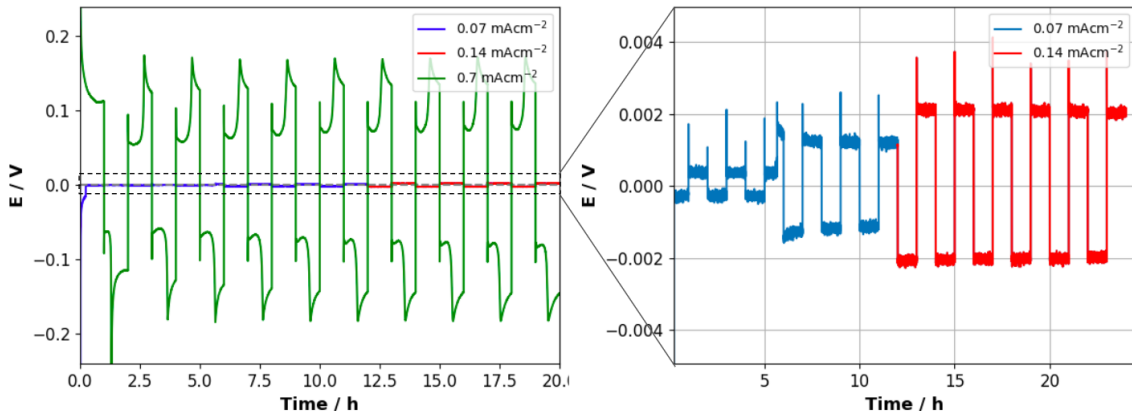


Figure B.1: Voltage profile of symmetric Na/Na cells cycled at 0.07 mA cm^{-2} , 0.14 mA cm^{-2} and 0.7 mA cm^{-2} , corresponding to charge rates of C/10, C/5 and 1C in the HC/Na half cells.

For the lower charge densities of 0.07 mA cm^{-2} and 0.14 mA cm^{-2} , a relatively low overpotential is observed. At the same time, high overpotentials peaking at 0.2 V can be seen when cycling at 0.7 mA cm^{-2} . Based on these results it was concluded that the charge rates C/5 and C/10 could be further used in this study, without the need for a three-electrode configuration, and that charge rates higher than C/5 would be left for future studies.

DEPARTMENT OF SOME SUBJECT OR TECHNOLOGY

CHALMERS UNIVERSITY OF TECHNOLOGY

Gothenburg, Sweden

www.chalmers.se



CHALMERS
UNIVERSITY OF TECHNOLOGY